TOWARDS INTENSE SINGLE ATTOSECOND PULSE GENERATION FROM A 400 *NM* DRIVING LASER

by

YAN CHENG

B.A., University of Science and Technology of China, 2009

A THESIS

submitted in partial fulfillment of the requirements for the degree

MASTER OF SCIENCE

Department of Physics
College of Arts and Sciences

KANSAS STATE UNIVERSITY
Manhattan, Kansas

2011

Approved by:

Co-Major Professor
Dr. Zenghu Chang

Approved by:

Co-Major Professor
Dr. Brian Washburn

Copyright

Abstract

Attosecond pulse generation is a powerful tool to study electron dynamics in atoms and molecules. However, application of attosecond pulses is limited by the low photon flux of attosecond sources. Theoretical models predict that the harmonic efficiency scales as λ^{-6} in the plateau region of the HHG spectrum, where λ is the wavelength of the driving laser. This indicates the possibility of generating more intense attosecond pulses using short wavelength driving lasers. The purpose of this work is to find a method to generate intense single attosecond pulses using a 400 *nm* driving laser. In our experiments, 400 *nm* femtosecond laser pulses are used to generate high harmonics. First, the dependence of the high harmonic generation yield on the ellipticity of 400 *nm* driving laser pulse is studied experimentally, and it is compared with that of 800 *nm* driving lasers. A semi-classical theory is developed to explain the ellipticity dependence where the theoretical calculations match experiment results very well. Next, 400 *nm* short pulses (sub-10 *fs*) are produced with a hollow core fiber and chirped mirrors. Finally, we propose a scheme to extract single attosecond pulses with the Generalized Double Optical Gating (GDOG) method.

Table of Contents

List of Figures

List of Tables

Acknowledgements

First and foremost I owe my deepest gratitude to my supervisor Dr. Zenghu Chang, who guided and supported me throughout my research with his knowledge, expertise and patience. I really learned a lot from him. He taught me to know the importance of focusing, the importance of understanding the real physics, and the importance of accumulation. He provided me an excellent example of being a physicist.

It is an honor for me to work with Sabih D. Khan, with whom I spent most of the time with in the lab. I finished almost all the experiment together with him, and I enjoyed working with him. From him I learned a lot of optics, electronics and programming knowledge. Dr. Baozhen Zhao and Dr. Kun (Harry) Zhao gave us a lot of good ideas, suggestions and support, with their help our experiment went on much more smoother. I also learnt how to tune the laser from them. Max Möller developed most of the high harmonic ellipticity dependence theory.

I would like to thank Dr. Brian Washburn, who is also my co-advisor, for his advice, his assistance and his great class. It is always a pleasure to have a discussion with Dr. Washburn. Dr. Washburn gave me a lot of help in writing and improve the thesis.

I further thank Dr. He Wang, Michael Chini and Dr. Shouyuan Chen. When I joined this group they taught me a lot of fundamental and useful experimental knowledge such as aligning optics, dealing with vacuum and etc.

I have been fortunate to have colleagues like Yi Wu, Qi Zhang and Yang Wang, they helped me in both research and life.

Additionally I would like to thank Dr. Brett D. DePaola for guiding me and serving on my committee.

Finally I would also like to show my gratitude to my parents Zesheng and Yuezhen, and my fiancée Dehui for their emotional support over the past years.

Chapter 1 - Introduction

High harmonics have the properties of superb spatial coherence and extremely short pulse duration on the attosecond time scale. These features have made high harmonic generation a good coherent short wavelength light source, opening new applications in nonlinear optics, holography and also in seeding free electron lasers [2]. Single attosecond pulses can be produced from high harmonic generation, and they are ideal tools for studying electron dynamics in atoms and molecules, and several experiments have been performed. However, the applications of isolated attosecond pulses have been limited by the low photon flux of the available attosecond sources. Usually we need to use a filter to block the fundamental driving pulses after generating single attosecond pulses. So far, the highest single attosecond pulse energy reported generated by an 800 nm driving pulsed laser after a filter is 2.1 *nJ*. This energy is too low for many applications, for example, the required single attosecond pulse energy for a helium two photon ionization experiment is estimated to be at least 10 *nJ*. However by using a 400 nm driving pulsed laser this energy can be obtained. This is primary reason for using a 400 nm driving laser over a 800 nm driving laser.

For further development of attosecond pulses applications, one of the most important issues is the improvement of high harmonics energy and conversion efficiency. In recent years, wavelength scaling of high harmonic yield has received much interest. Theoretical models predict that the high harmonic efficiency scales as λ^{-6} in the high harmonics plateau region, where λ is the wavelength of the driving laser. By using a shorter wavelength driving laser, the high harmonic generation efficiency can be significantly increased. So it is possible to generate intense single attosecond pulses with shorter driving laser wavelength. In this work, we will focus on using a 400 *nm* driving laser to generate high harmonics, and trying to find a scheme to produce single attosecond pulses from high harmonics with a 400 *nm* driving laser.

1.1 High harmonic generation

The high harmonic generation process has been studied extensively in recent years. It was first discovered by M. Ferray in 1988 [1]. By interaction of intense femtosecond lasers with a gas or solid target, an attosecond pulse train can be generated. In experiments, this is usually realized by focusing a femtosecond laser into a noble gas cell. This process can be understood with a semi-classical three step re-collision model which was developed in 1993 [2].

According to this model, in the first step the atom's potential is changed by the external laser field and the electron tunnels out. When the electron is freed from the atom, the electron wave packet responds classically and the released electron is accelerated in the external field. Then the electron recombines with its parent ion, and a high energy photon is produced. In the quantum mechanics point of view, the photon is produced by the interference of the bound electron wave packet and the returned electron wave packet [3]. Some of the electrons will return to the parent nucleus, with a maximum energy $3.17U_p + I_p$ [2], where U_p is the ponder-motive potential which is the average energy of the electron gained in a laser field, and I_p is the target atom ionization potential.

For a linearly polarized multi-cycle driving laser pulse, this process repeats every half a cycle of a laser period, which leads to the generation of an attosecond pulse train.

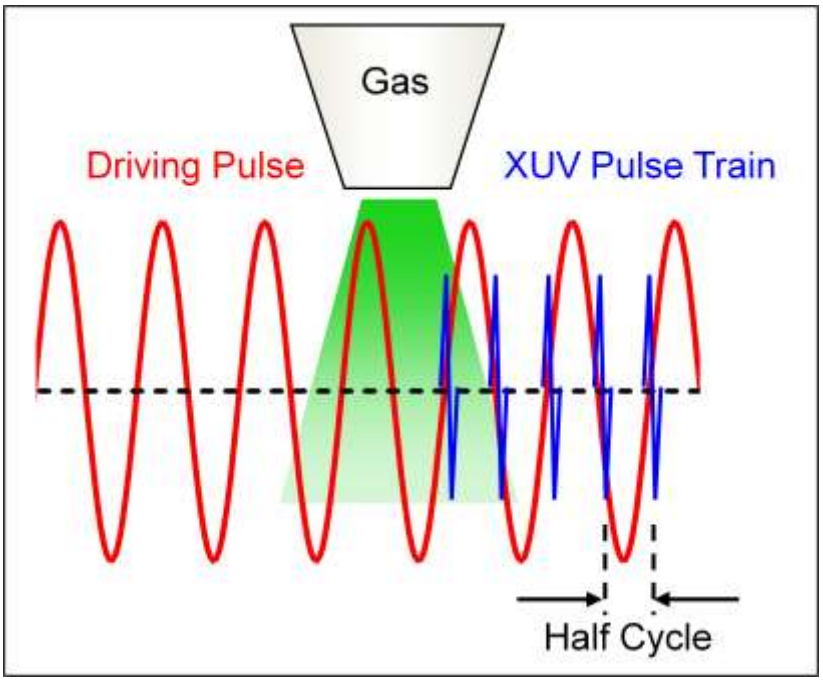

Figure 1-1 Attosecond XUV pulse train from a gas target

In the spectral domain, the attosecond XUV pulse train corresponds to a series of discrete high harmonics. The maximum electron returned energy predicts the cutoff of the high harmonics to be

$$E_{cutoff} = I_p + 3.17\frac{E_0^2 e^2}{4m\omega_0^2} \tag{1.1}$$

Here I_p is the ionization potential of the atom, E_0 is the driving laser field amplitude and ω_0 is the driving laser frequency. e is the electron charge and m is the electron mass.

1.2 High flux high harmonic generation

One of the limitations of high harmonic pulses is the low conversion efficiency of attosecond light bursts, especially for generating single attosecond pulses. High order harmonics have been generated with conversion efficiency of 10^{-4}-10^{-8}. Many schemes have been proposed and investigated to increase the conversion efficiency of the high harmonic generation process. These include phase matching [4] and reducing the driving laser wavelength [5].

In recent years, the role of driving laser wavelength to the HHG scaling received much interest. From numerical simulation, it is known that high harmonic generation efficiency scales as $\lambda^{-5}\sim\lambda^{-6}$ [6][7]. These simulation results are supported by several experiments [5]. Nowadays, the most commonly used Ti:sapphire laser's central wavelength is around 800 *nm*, which corresponds to an optical period of 2.67 *fs*. This theory gives us a hint that if the driving laser wavelength can be reduced to 400 *nm* the conversion efficiency can be significantly increased. For example, the Kärtner's group at MIT reported that they could reach a high harmonic generation conversion efficiency as high as 10^{-4}.

It is important to understand the wavelength scaling of high harmonic yield in using a semi-classical physical descriptions. It is important to note that a purely *classical* description will not explain the strong wavelength dependence since classical physics cannot provide a proper description of quantum tunneling, which is essential for HHG. According to the semi-classical strong field approximation (SFA) theory, the high harmonic yield scales as λ^{-3}[8]. This can be accounted for by the effect of the quantum diffusion of the electron wave packet. In the three-step model, high harmonics are generated by the recombination of released electrons and parent ions. The high harmonics field is proportional to the recombination probability, which is strongly affected by the overlap of the returning wave packet and the Coulomb potential [9]. The wave packet spreads with its propagation time τ as $\tau^{3/2}$, and for the high harmonic intensity this factor should be squared [8]. The propagation time τ is proportional to the driving laser wavelength, so the SFA theory concluded that high harmonics yield scales as λ^{-3}.

In 2007, Tate *et al.* [10] performed calculations using a numerical solution of the time dependent Schrodinger equation (TDSE). Surprisingly, it was found that the high harmonic yield followed a $\lambda^{-(5\sim6)}$ scaling at constant intensity, although they did not fully understand the physical origin of the stronger wavelength dependence.

Later in 2007, Schiessl *et al.* [11] performed another TDSE calculation where they found some more interesting results. The high harmonics yield did not smoothly decrease with fundamental wavelength but exhibited rapid oscillations with a period of 6-20 *nm* depending on the wavelength region. Their analysis revealed that the rapid oscillations were due to the interference of up to five different rescattering trajectories. When averaged over

the fast oscillations the high harmonics yield follows a λ^{-5} scaling, which is consistent with Tate *et al.* Unfortunately, they did not find a physical explanation for this scaling either.

In 2008, Frolov. *et al*. [12] described the high harmonic generation in terms of a system's complex quasienergy, and this reproduced the wavelength scaling predicted by Tate *et al.* and Schiessl *et al.* . They employed a time dependent effective range (TDER) theory to calculate HHG yield within the single active electron (SAE) approximation. They provided a qualitative explanation for the $\lambda^{-(5\sim6)}$ scaling. The λ^{-3} originated from the contribution of the least spreading, shortest classical trajectory. Those with longer return time and larger spreading contributed the cutoff region, thus leading to a value of larger than 3.

These theories were supported by experiments in 2009 by Shiner *et al.* [13]. They found that the scaling at constant laser intensity was $\lambda^{-6.3\pm1.1}$ in xenon and $\lambda^{-6.5\pm1.1}$ in krypton over the wavelength range of 800-1850 *nm*.

In 2009, Falcao-Filho et al. [6] calculated the closed form expressions for the high harmonic generation conversion efficiency for the plateau and cutoff regions. The SAE approximation was used, and multielectron effects were partially included using the recombination amplitude computed via the Hartree-Slater potential approach. They concluded that the scaling of high harmonic generation efficiency with the driving wavelength was λ^{-5} at the cutoff and λ^{-6} at the plateau region.

The figure below is a comparison between high harmonics driven by the 800 *nm* pulse and by the 400 *nm* pulse. Here we can see that high harmonics from the 400 *nm* driving pulse is around 12 times stronger than that from the 800 *nm* driving pulse. Details of the experiments will be discussed later. Due to the λ^{-6} wavelength dependence one may expect a 64 times increase in HHG. This HHG conversion efficiency was not obtained since at 400 *nm* we could not obtain the same pulse energy as at 800 *nm* due to the 25% SHG conversion efficiency. In spite of this using a 400 nm driving laser is still more advantageous than using an 800 nm driving laser because the 400 nm laser will generate a larger HHG pulse energy. Since our SHG conversion efficiency is 25% and the improvement in HHG conversion efficiency due to the λ^{-6} wavelength scaling is 2^6 or 64.

Thus by using a 400 nm driving laser the total HHG energy will be $0.25 \times 64 = 16$ times larger. This corresponds well with the 12 times enhancement we measured as seen below.

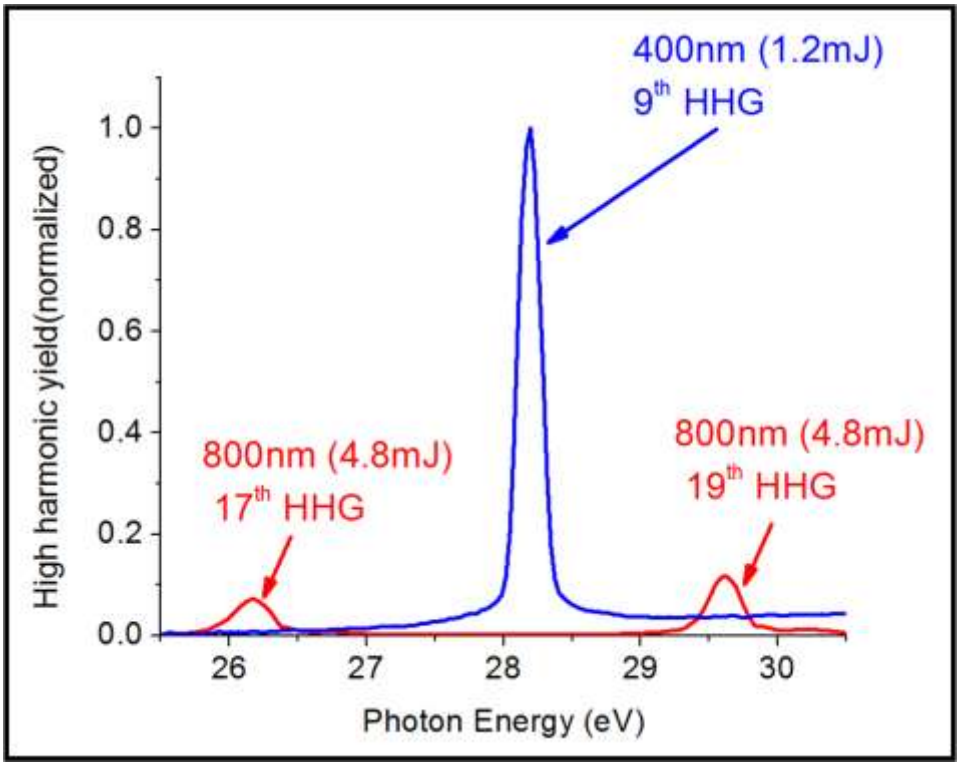

Figure 1-2 High harmonics generated from 800 *nm* driving pulses and 400 *nm* driving pulses

1.3 Single attosecond pulse generation methods

While an attosecond pulse train is very useful there is great interest and need to generate an isolated single attosecond pulse for a variety of novel experiments studying ultrafast phenomenon. For example, with single attosecond pulses one can perform pump-probe experiments of atomic and molecular systems with attosecond resolution [14].

Currently there are several gating schemes to generate single attosecond pulses. These include Polarization Gating (PG) [15,16], Double Optical Gating (DOG) [17,18], Generalized Double Optical Gating (GDOG) [19] and others.

P. Corkum proposed an approach to generate isolated single attosecond pulses in 1994 known as the polarization gating (PG) [20]. This gating method is based on the fact that the high harmonic generation efficiency strongly depends on the ellipticity of the driving pulses. High harmonic generation efficiency is highest when the driving laser is linearly polarized. As the ellipticity of the driving pulse increases, the high harmonic efficiency drops significantly, and it is lowest when the driving laser ellipticity is 1. For our experiments we can use a quartz plate and a quarter wave plate to produce a pulse which is circularly polarized in the leading and trailing edges and linearly polarized in the center part.

The PG requires a very short driving pulse; in the case of 800 *nm* driving lasers the required driving pulse duration is 6.6 *fs*. This is difficult to achieve in the laboratory on a daily basis. So far, the shortest single attosecond pulse generated by polarization gating is 130 *as*, with energy of around 70 pJ in the spectral range of 25-50 *eV* [15]. As the laser pulse duration increases, the conversion efficiency from driving laser pulse to attosecond pulse decreases.

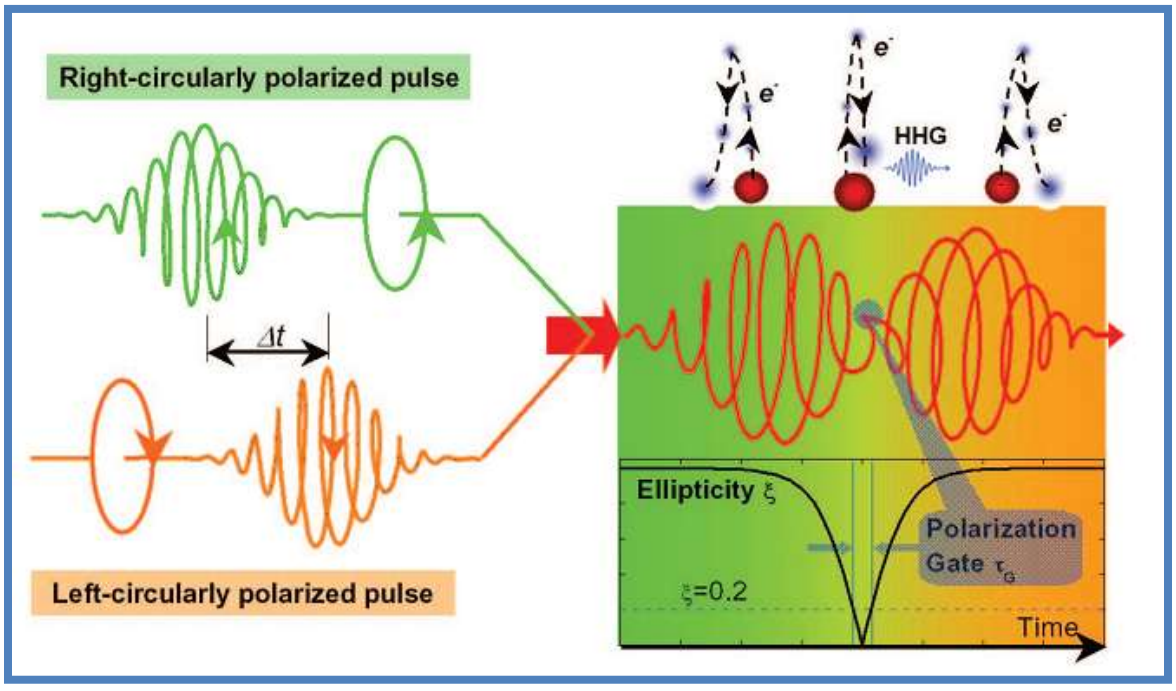

Figure 1-3 Polarization Gating scheme, two counter rotating circularly polarized pulse are combined with a delay, in the centered part of the combined pulse it is linearly polarized, in the heading and trailing part it is circularly polarized. From [21]

Another method for generating isolated attosecond pulses is the Double Optical Gating (DOG). In double optical gating, a second harmonic is added to the fundamental driving laser, so that the symmetry of the driving laser is broken. The high harmonic generation process occurs only once every cycle, not once every half a cycle as in the polarization gating. Using such a two color scheme, the polarization gate can be one optical cycle. The advantage of this method is that it allows us to generate single attosecond pulses with driving laser pulse duration up to 12 *fs*.

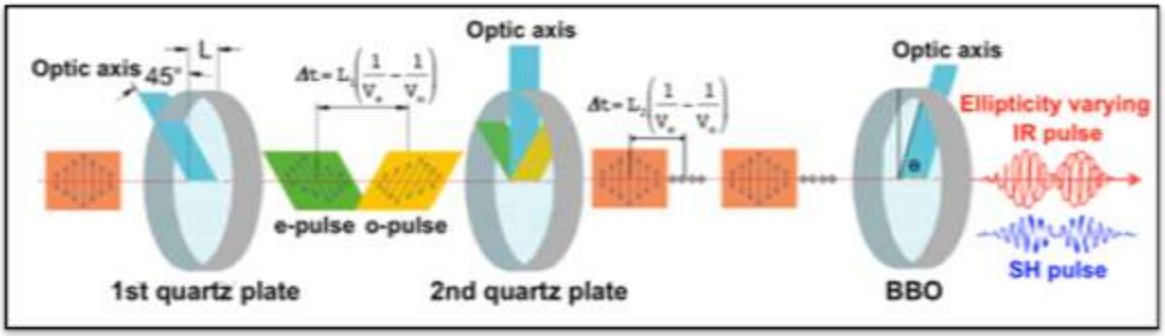

Figure 1-4 Double Optical Gating. From [22]

The Generalized Double Optical Gating (GDOG) technique can generate single attosecond pulses from sub-30 *fs* driving pulses. By adding a Brewster window to the double optical gating setup, the ellipticity of the driving pulse is reduced and thus the ground state gas population depletion can be reduced. This makes single attosecond pulses achievable in most femtosecond laser labs.

1.4 Overview of the thesis

The overall goal of the thesis is to find an approach to generate intense single attosecond pulses using a 400 *nm* driving laser. First I will discuss the ellipticity dependence of high harmonics from both 400 *nm* driving pulses and 800 *nm* driving pulses. Knowing the high harmonic ellipticity dependence is of great importance for gating. Based on the ellipticity result, we will calculated the required temporal gating (PG, DOG, GDOG) parameters. From the experimental results we found that we can implement GDOG to produce single attosecond pulses with 400 *nm* driving pulses while it is not possible to use

PG. To use GDOG, a 6.5 *fs* 400 *nm* driving laser is needed. In the next part I will show how we generated the sub-10 *fs* 400 *nm* short pulse. A 400 *nm* GDOG scheme will be proposed at the end. Chapter 4 will discuss the applications of the attosecond pulses for novel experiments in ultrafast physics such as the attosecond dynamics of autoionization in argon. I will focus on the XUV spectrometer used in the experiments. I will conclude with a short summary and the future plan.

Chapter 2 - Ellipticity dependence of 400 *nm* driven high harmonics

Ellipticity dependence of the high harmonic yield is the foundation for designing temporal gating schemes to extract a single isolated attosecond pulse. As discussed in Chapter 1, in order to find the right gating scheme to generate isolated single attosecond pulses from a 400 *nm* driving laser, the first step should be to find the ellipticity dependence of the high harmonics from 400 *nm* driving lasers. In this chapter, the experimental result of ellipticity dependence of the 400 *nm* driven high order harmonics will be discussed and compared with the result from the 800 *nm* driving laser. When the driving pulse is elliptically polarized, the returned electron is driven away from its parent ion by the transverse electric field component, so the high harmonic yield drops significantly as the driving laser ellipticity increases. Also, a semi-classical model to calculate the yield of high harmonics from elliptically polarized driving pulses will be presented. Based on the result of the 400 *nm* high harmonics ellipticity dependence, we will discuss the feasibility of different gating schemes to extract isolated single attosecond pulses from 400 *nm* driving lasers.

2.1 Experimental Setup

The experiments are carried out in the Manhattan Attosecond Radiation Source (MARS) laser facility, which is a two stage laser amplifier including a regenerative amplifier and a single pass amplifier (Coherent Legend Elite Duo TM). The laser system outputs 4.8 *mJ*, 35 *fs* pulses with a central wavelength of 800 *nm* at 1 *kHz*.

We generate a 400 *nm* pulse by frequency doubling the 800 *nm* pulses from MARS laser with a 300 μm thick beta barium borate (BBO, Type I phase matching at $\theta = 29.2°$) crystal . With this fundamental pulse, we can get a 1.2 *mJ* 400 *nm* pulse with a conversion efficiency of 25%. To increase the conversion efficiency, the input 800 *nm* pulse is

negatively chirped by changing the laser compressor gratings distance, so as to pre-compensate the dispersion of the BBO crystal.

The 400 *nm* pulse is separated from 800 *nm* with two LWP dichroic mirrors (reflect 400 *nm* pulses and transmit 800 *nm* pulses). The dichroic mirrors are from the FemtoLasers company (OA075, 6.35 *mm* thick). The following curve shows the reflectivity of the dichroic mirrors at different wavelengths.

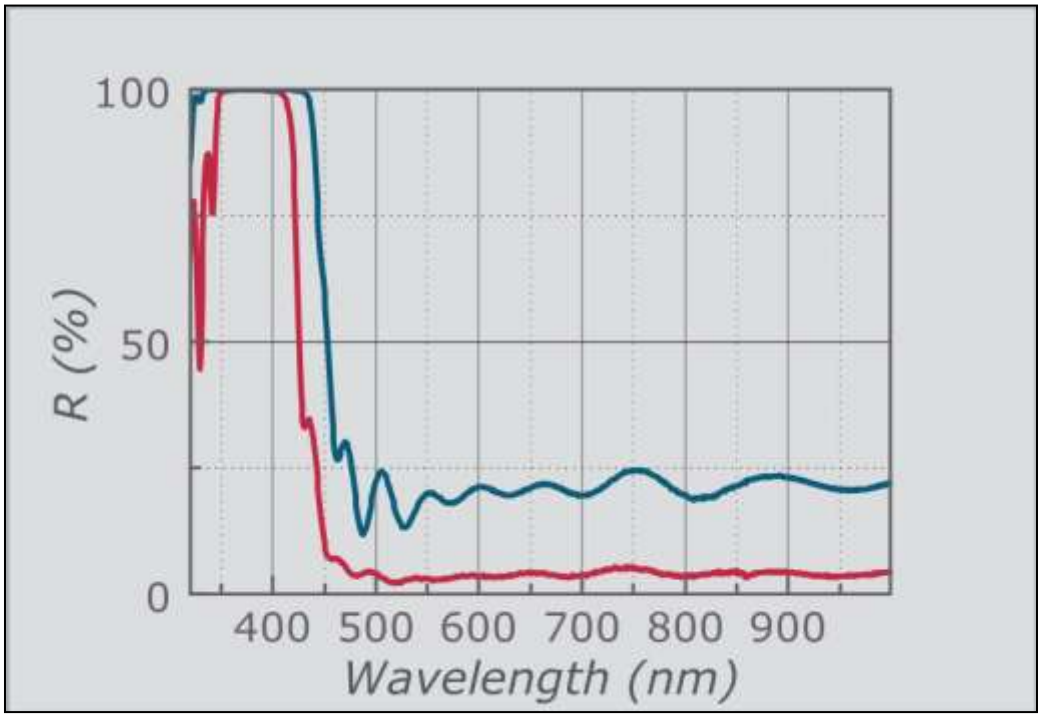

Figure 2-1 The reflectivity of the dichroic mirrors. From FemtoLasers catalog, blue: s-polarized light, red: p-polarized light (http://www.femtolasers.com/fileadmin/documents/Leaflets/FEMTOOPTICS.pdf)

One practical issue in choosing the dichroic mirrors is that it is necessary to use a thick substrate mirror. At the beginning of our experiments, we were using 1 *mm* thick dichroic beam splitters, and we found that there was astigmatism when we focused the beam. A Z-scan was done to see the astigmatism as seen in the CCD image below.

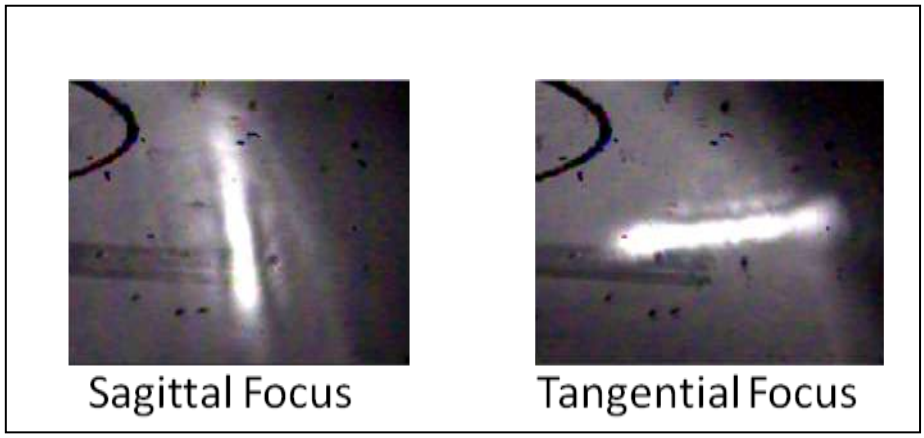

Figure 2-2 Z-scan of the focused 400 *nm* pulse when using 1 *mm* thin dichroic beam splitter. Astigmatism was observed.

Unfortunately we were not able to get rid of the astigmatism after careful optimization. The astigmatism was finally removed when we increased the thickness the dichroic mirrors (FemtoLasers, OA075, 6.35 *mm* thick). We concluded that the reason for the astigmatism was that the previous dichroic beam splitters were too thin, and when mounted, the surface of the beam splitter became distorted and this brought astigmatism to the focused beam.

The spectrum of the generated 400 *nm* pulse is shown below. We measured it with an Ocean Optics spectrometer. The pulse is centered at 405 *nm* with a full-width at half maximum (FWHM) bandwidth of 7 *nm*.

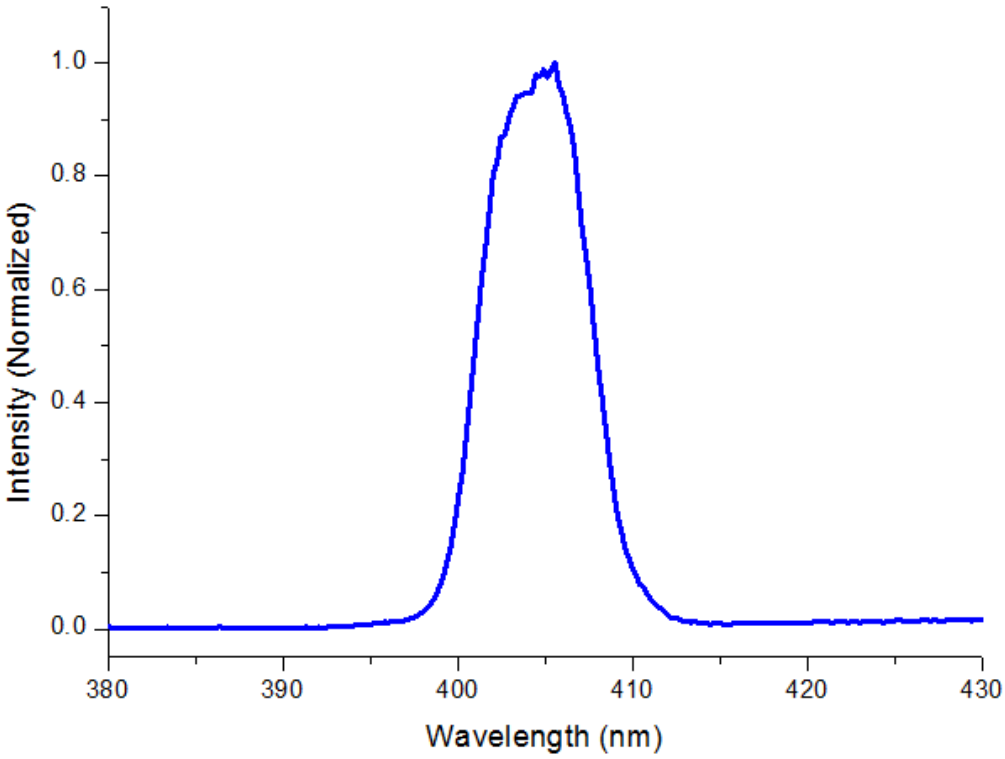

Figure 2-3 400 *nm* long pulse spectrum, the spectrum is centered at 405 *nm* with FWHM 7 *nm*.

The experimental setup used to measure the 400 *nm* HHG ellipticity dependence is shown in the following figure. 800 *nm* laser pulses from MARS laser passed through a 300 μm BBO to generate 400 *nm* light. Two dichroic mirrors that reflect the 400 *nm* laser and transmit the 800 *nm* laser were used to remove the fundamental 800 *nm* pulse. After the dichroic mirrors, a half wave plate and a quarter wave plate were used in combination to adjust the ellipticity of the input laser [23]. In the experiment, the quarter wave plate was fixed with its optic axis along the dispersion direction of the grating, and we changed the ellipticity by rotating the half wave plate only so that the major axis of the elliptical polarization did not change. The major axis was along the grating dispersion direction. By doing this, we can minimize the effect of the polarization dependent diffraction efficiency of the grating.

Next the 400 *nm* pulse was focused in to a gas cell target with a 375 *mm* concave mirror. The gas cell was 1.5 *mm* inner diameter, so the length of the gas target was 1.5mm. After the gas cell, a 300*nm* thick aluminum filter (Lebow Company) was used to remove the fundamental 400 *nm* laser leaving only XUV light. The filter was mounted on a gate valve and was also used for differential pumping, which separates the low pressure multi-channel plate (MCP) detector side from the high pressure HHG chamber side. For the safety of the MCP detector, the pressure in the MCP chamber was usually maintained at 3×10^{-7} *Torr*, the pressure in the MCP chamber should never be higher than 5×10^{-6} *Torr*. The background pressure in the HHG chamber is around 5×10^{-4} *Torr*.

The XUV beam was incident on a toroidal grating (384 lines/mm, Jobin Yvon Horiba 541-00-120), and we used a micro channel plate detector (MCP) with a phosphor screen (25 μm pore size, Burle 3075FM) as the detector. A voltage of -1600 *V* was applied on the MCP and 2200 *V* on the phosphor screen. The HHG spectrum image was recorded with a cooled CCD camera (Andor LUCA with EMCCD).

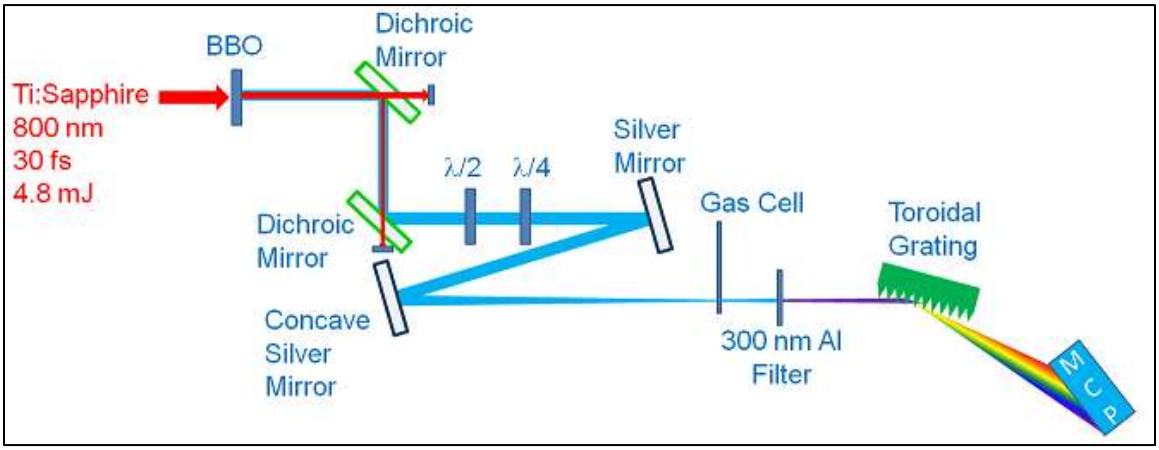

Figure 2-4 Experiment setup for measuring the HHG ellipticity dependence from 400 *nm* driving laser [24]

In the case of measuring the high harmonics ellipticity dependence from 800 *nm* driving laser, we used the same setup. The difference was that 800 *nm* pulses from the MARS laser were used directly, and the ellipticity was changed with a combination of an 800 *nm* half wave plate and an 800 *nm* quarter wave plate.

Care must be taken in choosing the appropriate filters. The filters should be able to block the fundamental 800 *nm* and 400 *nm* driving laser, while transmitting as much XUV light as possible. In this case aluminum is a good option as seen in the transmission curve of below. The transmission range is from 15 eV to 72 eV, which corresponds to 9^{th} and 45^{th} harmonics of the 800 *nm* driving laser. This range is sufficient for our current experiment.

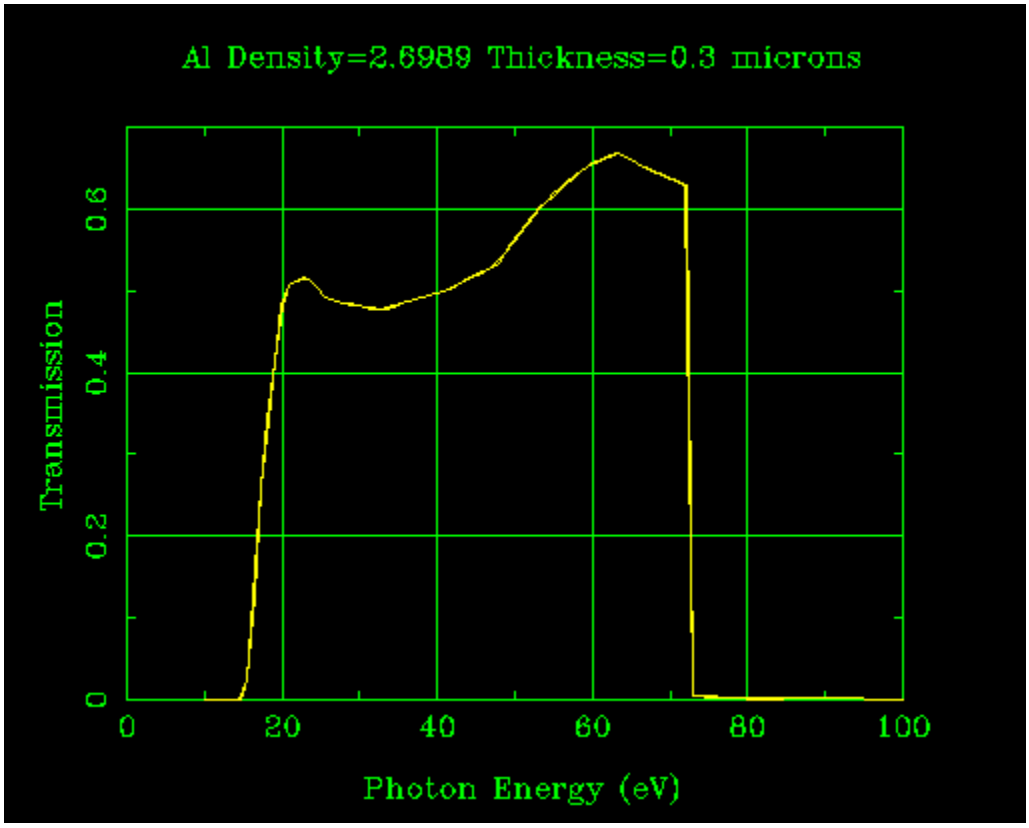

Figure 2-5 Al filter transmission curve, from
http://henke.lbl.gov/optical_constants/filter2.html

2.2 High harmonics from a 400 *nm* driving laser

It has been theoretically [6,25] and experimentally [5] demonstrated that high harmonics from 400 *nm* driving lasers are much more efficient by two orders of magnitude

than that from 800 *nm* driving lasers. Kim et. al [26] also reported that by applying a high intensity second harmonic driving pulse in addition to the 800 *nm* laser, the high harmonics generated in both orthogonally polarized and parallel polarized two-color field are stronger than that from the fundamental driving laser only by more than two orders of magnitude.

Many factors will affect the high harmonic yield, and there are several approaches to increase the high harmonics photon flux. The phase matching technique [27] is a good way to optimize the high harmonic flux. Phase matching is affected by many factors, such as the location of the gas target in the laser focus region, the gas pressure and other factors [4]. The high harmonic photon flux that can be achieved is determined by the balance between the coherence length, the absorption length and the medium length [4]. The ideal situation of phase matching is that all the high harmonic fields emitted by atoms located at different positions are in phase with the driving laser so that the generated photons add up constructively and the photon flux is maximized. In other words, the wave vector mismatch Δk is zero, where Δk is defined as the phase difference between the driving laser and the high harmonics. So, to further increase the 400 *nm* HHG intensity we optimized it by scanning the gas pressure and the gas cell position to find the best condition to generate high harmonics.

We compared the 400 *nm* high harmonics with 800 *nm* high harmonics. According to theory [6] the HHG harmonic conversion efficiency due to the single atom response scales as λ^{-6}, thus the 400 *nm* HHG conversion efficiency is 64 times higher than HHG from 800 *nm* driving laser. High harmonics were produced using 400 *nm* and 800 *nm* driving laser respectively. In both cases, the input driving laser pulse energy was 0.86 *mJ* for a neon gas target. The voltage on the MCP detector was the same in both cases so as to compare the high harmonic yields directly.

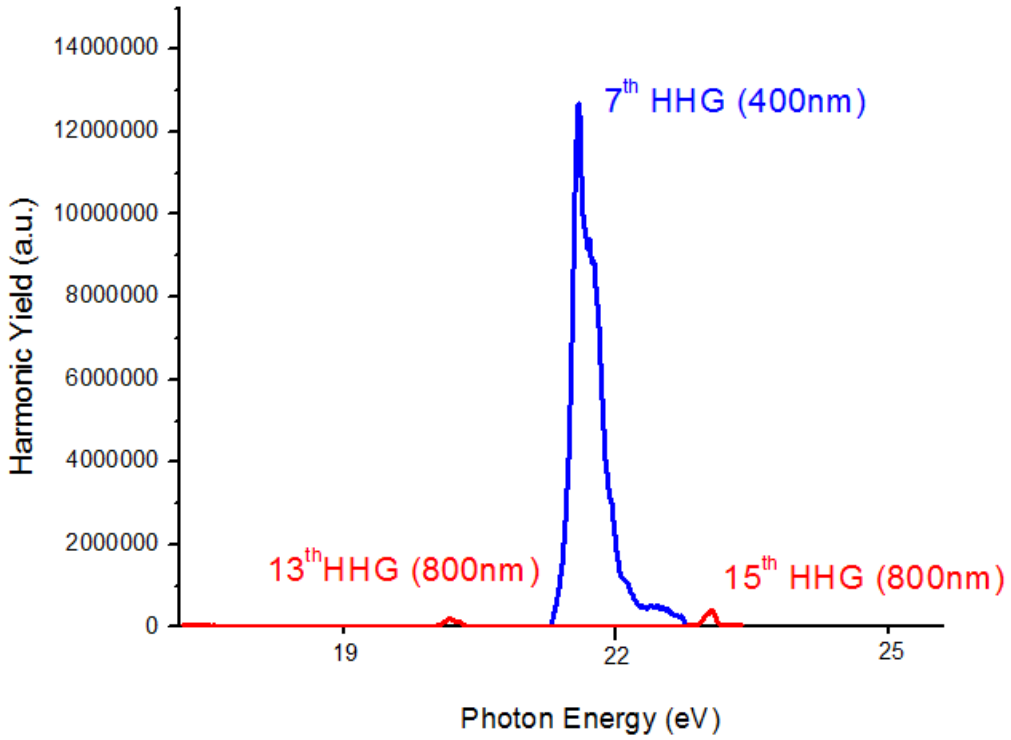

Figure 2-6 High harmonics from different wavelength driving laser: Blue - the 400 *nm* driving laser, Red - the 800 *nm* driving laser. The pulse energy are both 0.86 *mJ*. The gas target is Ne.

From this result under the same driving laser energy, we can get the conversion efficiency ratio of 400 *nm* and 800 *nm* driving laser of 187.

It is critical to determine the real driving laser intensity at the target gas. In our experiment, we needed to switch between 400 *nm* driving laser and 800 *nm* driving laser. We cannot measure the laser power at the gas target directly; we can only measure it before the folding mirror. After the folding mirror, there is an aluminum focus mirror and a 400 *nm* anti-reflection (AR) coated fused silica window, its reflectivity for 400 *nm* and 800 *nm* laser is different, so theoretical calculation is not very accurate. We developed the following method to determine the real intensity at the gas target. The cutoff high harmonic energy is given by

$$E_{cutoff} = I_p + 3.17\frac{E_0^2 e^2}{4m\omega_0^2} = I_p + 3.17 \times 9.33 \times 10^{-14} I_L \lambda_0^2, \quad (2.1)$$

Here I_p is the ionization potential of the atom, E_0 is the driving laser field amplitude and ω_0 is the driving laser frequency, e is the electron charge and m is the electron mass. I_L is the intensity of the laser in W/cm^2, and λ_0 is driving laser wavelength.

For a certain harmonic order N its energy is given by $N\hbar\omega_0$. Then we reduce the driving laser power to a certain point (power measured as P_N) that the N^{th} harmonic just disappeared, this means the corresponding laser intensity is

$$I_L = \frac{N\hbar\omega_0 - I_p}{3.17 \times 9.33 \times 10^{-14} I_L \lambda_0^2}, \quad (2.2)$$

so we have the relation

$$P_N \leftrightarrow I_L = \frac{N\hbar\omega_0 - I_p}{3.17 \times 9.33 \times 10^{-14} I_L \lambda_0^2}, \quad (2.3)$$

We also know that the power is proportional to the laser intensity, so when the driving laser power is P_0, the corresponding laser intensity at the gas target is

$$I_0 = \frac{P_0}{P_N} \times I_L \quad (2.4)$$

giving the real intensity at the gas target when the power is changed. This method works for both 400 *nm* driving lasers and 800 *nm* driving lasers.

It is worthwhile to mention how to control the driving laser pulse energy. It is very important since we did our experiments under many different driving laser intensities. For the 400 *nm* driving laser, the BBO phase matching angle can be tuned and the driving pulse energy will reduce. It is more complicated for 800 *nm* driving pulses. During the experimental process, we found that we could not use a variable neutral density (ND) filter to control the intensity, because the filter became heated and distorted. This caused the beam profile of the driving laser to change, and the high harmonic yield decreased. A better way to reduce driving laser intensity is to use a combination of half wave plate and polarizer. We fixed the polarizer with its optic axis along the laser polarization then placed the half wave plate before the polarizer. By rotating the half wave plate, we could control the driving laser intensity.

2.3 Semi-classical model for high harmonics ellipticity dependence

We developed a semi-classical model to explain the ellipticity dependence of high harmonics [28]. The model is based on the assumption that, in an elliptically polarized driving field, the major contribution to the high harmonic generation comes from electron trajectories in which the transverse displacement is compensated by an initial electron transverse velocity. Electrons from these trajectories have a higher possibility to recombine with the parent ion and produce high harmonic generation.

An electric field with ellipticity ε can be expressed as

$$\vec{\mathcal{E}}(t) = E_{x0}[\boldsymbol{i}\cos(\omega_0 t) + \boldsymbol{j}\,\varepsilon sin(\omega_0 t)], \tag{2.5}$$

Here the major axis is defined as along the x direction and the minor axis along the y direction. E_{x0} is the amplitude of the major axis, $\boldsymbol{i}$ and $\mathbf{j}$ are unit vectors in the x and y directions respectively. So the minor axis amplitude can be written as εE_{x0}.

Total electric field amplitude

$$E_0 = \sqrt{E_{x0}^2 + E_{y0}^2} = E_{0x}\sqrt{1+\varepsilon^2}. \tag{2.6}$$

We know that for an electric field amplitude, laser intensity $I = \frac{1}{2}c\varepsilon_0 E_0^2$, so

$$E_{x0} = \sqrt{\frac{2I}{c\epsilon_0}}\frac{1}{\sqrt{1+\varepsilon^2}} \tag{2.7}$$

When the electron is freed by tunneling, the effect of the parent ion's Coulomb field can be neglected, and the electron is then only affected by the external laser field. Using Newton's 2nd Law, the electron's motion in the x and y directions can be written as

$$m_e\frac{d^2x}{dt^2} = -eE_{x0}\cos(\omega_0 t), \tag{2.8}$$

$$m_e\frac{d^2y}{dt^2} = -e\varepsilon E_{x0}\sin(\omega_0 t). \tag{2.9}$$

Solving these equations, we can get

$$x(t) = -\frac{E_0}{\sqrt{1+\varepsilon^2}}\frac{1}{\omega^2}[-\cos\omega t + \cos\omega t_0 - \omega(t-t_0)\sin\omega t_0] + (t-t_0)v_{x0}, \tag{2.10}$$

$$y(t) = -\frac{E_0}{\sqrt{1+\varepsilon^2}}\frac{1}{\omega^2}[\varepsilon(-\sin\omega t + \sin\omega t_0 + \omega(t-t_0)\cos\omega t_0)] + (t-t_0)v_{y0}. \tag{2.11}$$

Here v_{x0} and v_{y0} are the initial velocity of the electron when it is freed, t_0 is the time when the electron is released, and the initial position of the electron is set to zero.

We define α_0 as the angle between the ionization field vector and the coordinate axis

$$\alpha_0 = \tan^{-1}(\varepsilon \tan(\omega t_0)) \tag{2.12}$$

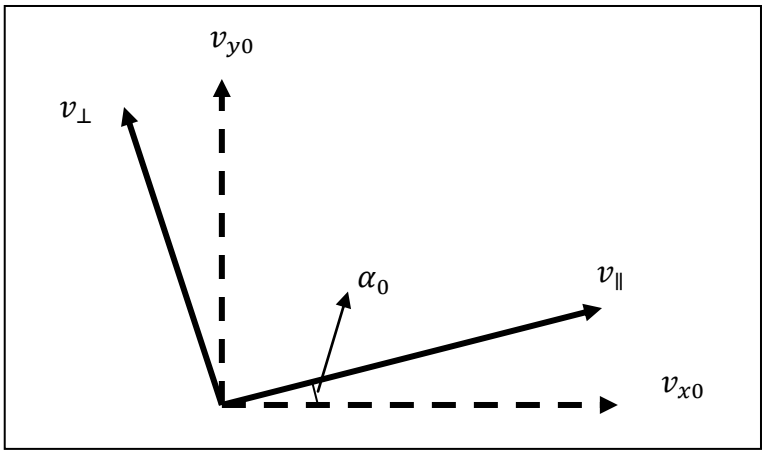

Figure 2-7 Angle between the ionization field vector and the coordinate axis

We assume that parallel velocity $v_\parallel$ is equal to zero. When ellipticity $\varepsilon \neq 0$, and initial velocity $v_\parallel = v_\perp = 0$, there is no chance that the electron can recombine with its parent ion, as illustrated in the figure below with $v_\perp = 0$. However, if the initial perpendicular velocity is not zero, $v_\parallel \neq 0$, it is possible that at a later time t_r the electron returns to the parent ion.

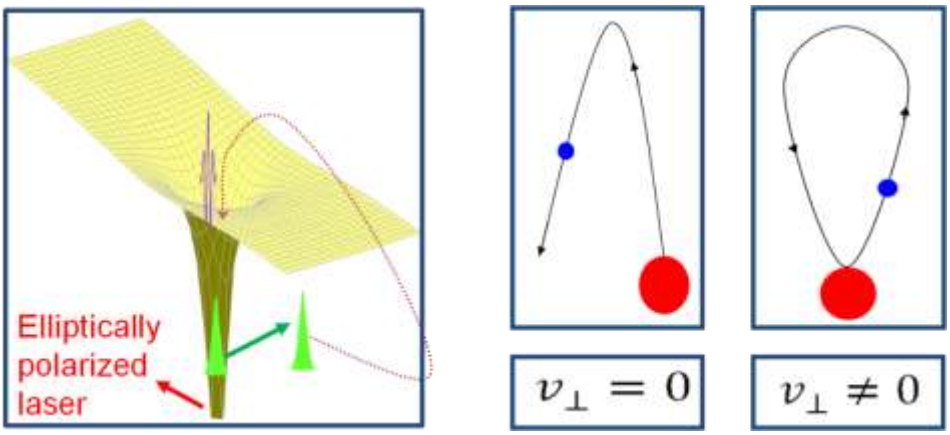

Figure 2-8 Electron trajectories in elliptically polarized fields, when the initial transverse velocity is zero, the electron can never recombine with the parent ion; when the initial transverse velocity is not zero, it is possible that for a certain transverse velocity, the electron can recombine with the parent ion.

For this to occur, it requires that

$$x(t_r) = y(t_r) = 0, \tag{2.13}$$

so we can get

$$\begin{aligned}(\varepsilon^2+1)\omega(t_r-t_0)\sin\omega t_0\cos\omega t_0 - \varepsilon^2\sin\omega t_0(\sin\omega t_r - \sin\omega t_0) + \\ \cos\omega t_0(\cos\omega t_r - \cos\omega t_0) = 0,\end{aligned} \tag{2.14}$$

and we can find the initial velocity

$$v_\perp = -\frac{E_0\varepsilon}{\sqrt{1+\varepsilon^2}}\frac{1}{\omega\cos\alpha_0}\left(\frac{\sin\omega t_r - \sin\omega t_0}{\omega(t_r-t_0)} - \cos\omega t_0\right). \tag{2.15}$$

From theory[29] we know that high harmonics yield of a elliptically driving field with respect to the yield of a linearly polarized driving field can be written as

$$\frac{I_{XUV}(\varepsilon)}{I_{XUV}(\varepsilon=0)} \approx \frac{w(v_\perp)}{w(v_\perp=0)} = \exp\left(-\frac{\sqrt{2I_p}v_\perp(\varepsilon)^2}{|E_0(t_0)|}\right), \tag{2.16}$$

here $w(v_\perp)$ is the perpendicular velocity distribution.

When ellipticity of the driving field is small, $\varepsilon^2 \ll 1$, $\sqrt{1+\varepsilon^2} \approx 1$, we can get

$$\frac{I_{XUV}(\varepsilon)}{I_{XUV}(\varepsilon=0)} \approx \exp\left(-\frac{\beta^2\sqrt{2I_pI}}{4\pi^2c^2}\lambda^2\varepsilon^2\right), \tag{2.17}$$

Defining ε_{th} as the ellipticity where the high harmonic yield drops to 10% of the maximum yield

$$\varepsilon_{th} \approx \frac{691}{{I_p}^{1/4}}\frac{1}{I^{1/4}}\frac{1}{\lambda}, \tag{2.18}$$

From this equation we can see that ε_{th} depends on the atom's ionization potential, the driving laser intensity, and the driving laser wavelength. We will compare the calculation with our experiment result.

2.4 Experiment Result and Discussion

In this section the experimental results will be presented and discussed.

2.4.1 High harmonics ellipticity dependence

Ellipticity dependence of high harmonics with 400 *nm* and 800 *nm* driving pulses were measured, and they are compared with the semi-classical theory calculation results.

In the figure below, we show the ellipticity dependence of high harmonics of 400 *nm* and 800 *nm* driving lasers. The results are measured with a peak intensity of $2.7 \times 10^{14}\ W/cm^2$ with an argon gas target. From this result we can see that the high harmonic yield from the 800 *nm* driving laser drops faster with increasing ellipticity than that from the 400 *nm* driving laser.

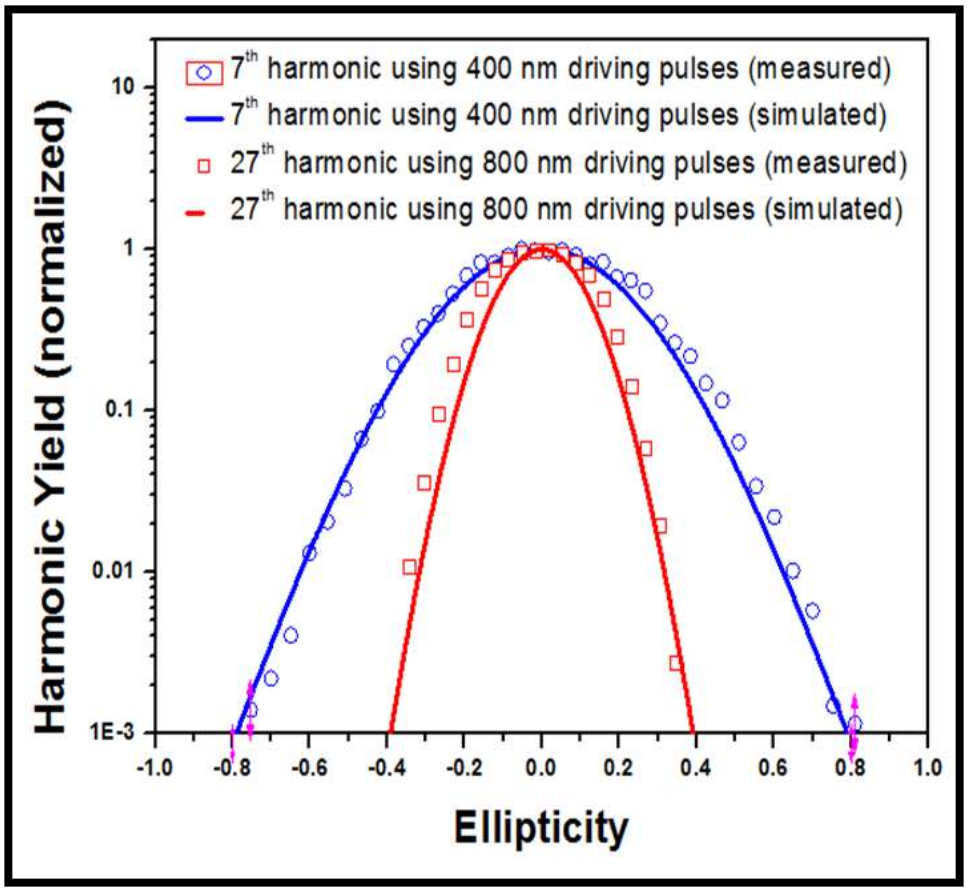

Figure 2-9 Harmonic yield as a function of ellipticity for the 27th harmonic using 800 *nm* driving laser (square) fitted with theoretical calculation (dashed line) and 7th harmonic using 400 *nm* driving laser (circle) fitted with theoretical calculation (solid line). Peak Intensity for both cases was 2.7×10^{14} *W/cm*^{2}. While performing the experiments, for each data point, the experiment was repeated for 20 times. The error bar was estimated by the fluctuation of high harmonic yield. The error bar of the ellipticity can be estimated from the error of the half wave plate rotation, which is 0.5 degree.

In the next figure, the ellipticity dependence of high harmonics of 400 *nm* and 800 *nm* driving laser is shown. The results are measured with a peak intensity of $7.7 \times 10^{14}\ W/cm^2$ with a helium gas target. The threshold ellipticity (see the previous section for definition) ε_{th} is 0.31 and 0.21 for the 400 *nm* laser and the 800 *nm* laser respectively. From this result we can see that the high harmonic yield from the 800 *nm* driving laser drops faster with increasing ellipticity than that from the 400 *nm* driving laser. The numerical results match the experiments quite well.

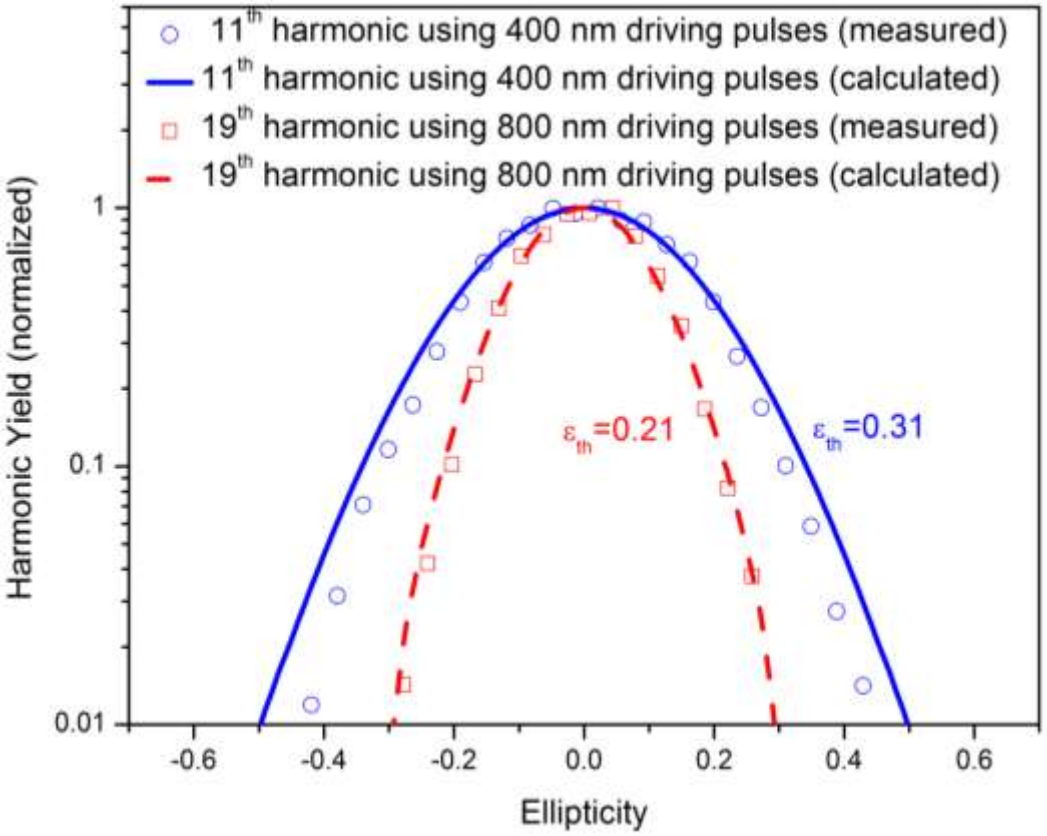

Figure 2-10 Normalized harmonic yield as a function of ellipticity in helium for the 19th harmonic using the 800 *nm* driving laser (squares) and the 11th harmonic using the 400 *nm* driving laser (circle). Peak intensity for both cases was 7.7x10^{14} *W/cm*^{2}. The results from semi-classical calculations using the experimental parameters are shown for comparison (solid and dashed lines for 400 *nm* and 800 *nm* respectively). From [24]

2.4.2 PG/DOG/GDOG parameters and considerations

For polarization gating, the driving laser is created by composing two counter-rotating fields, the leading and trailing edge of the pulse are circularly polarized, in the center part the pulse is linearly polarized, the width of the gate where the driving laser are considered linearly polarized can be expressed as

$$\delta t = \frac{\alpha}{\ln(2)} \varepsilon_{\mathrm{th}} \frac{\tau_{\mathrm{p}}^2}{T_{\mathrm{d}}} \tag{2.19}$$

here ε_{th} is defined as the ellipticity where the harmonic yield dropped by 10%. τ_P is the pulse duration of the pulse (fs) and T_d is the delay between the two counter rotating electric fields. α is 1 for PG and DOG, and for GDOG, α is 0.5.

Using these equations, we calculated the required time delay T_d for 400 *nm* driving laser as a function of pulse duration. For PG, the delay δt is set to half an optical cycle and for DOG and GDOG, the time delay δt is set to a full optical cycle in order to extract a single isolated attosecond pulse from the high harmonic pulse train.

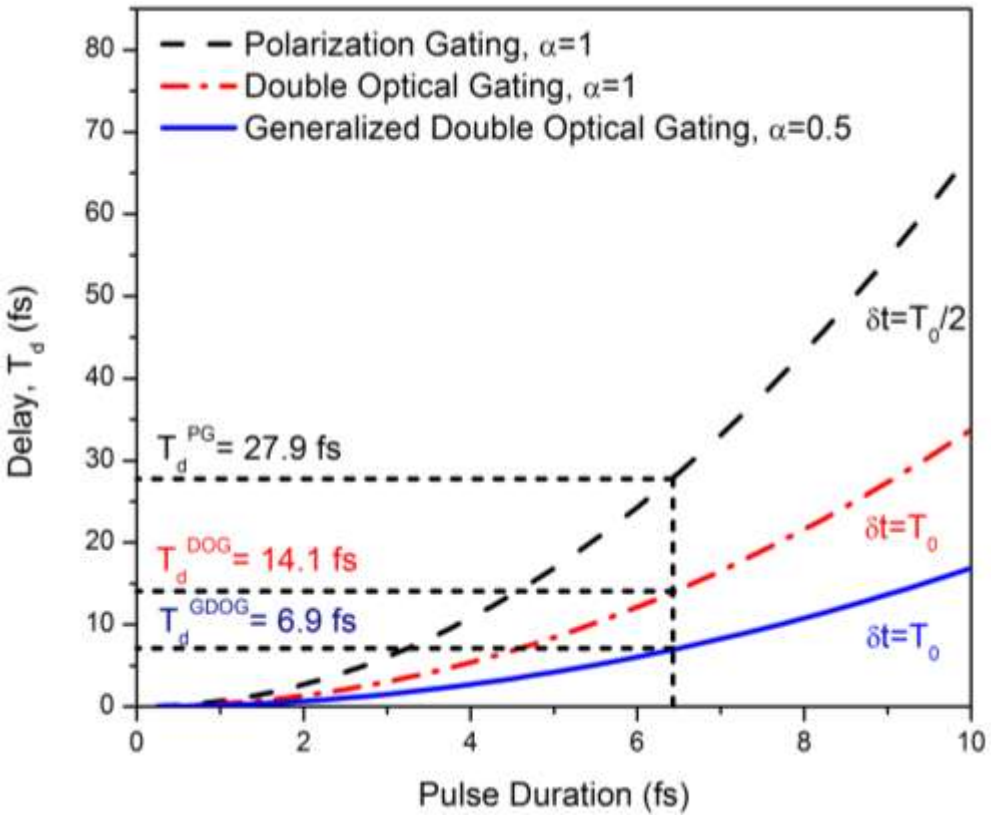

Figure 2-11 Comparison of delay T_d as a function of pulse duration. From [24]

From the result we can see that, for polarization gating, a 6.5 *fs* driving pulse requires a delay between counter rotating elliptically polarized pulses of 27.9 *fs* in order to keep the gate width at half of a cycle period. This separation results in no overlap within the gate, and the intensity will not generate an attosecond pulse. Therefore polarization gating will not efficiently generate an isolated single attosecond pulse from 400 *nm* driving laser. In

contrast, the required delay time for GDOG is 6.9 *fs*, which is comparable to the driving laser pulse duration.

We also estimated the ground state depletion by using the Ammosov-Delone-Krainov (ADK) [30] rate.

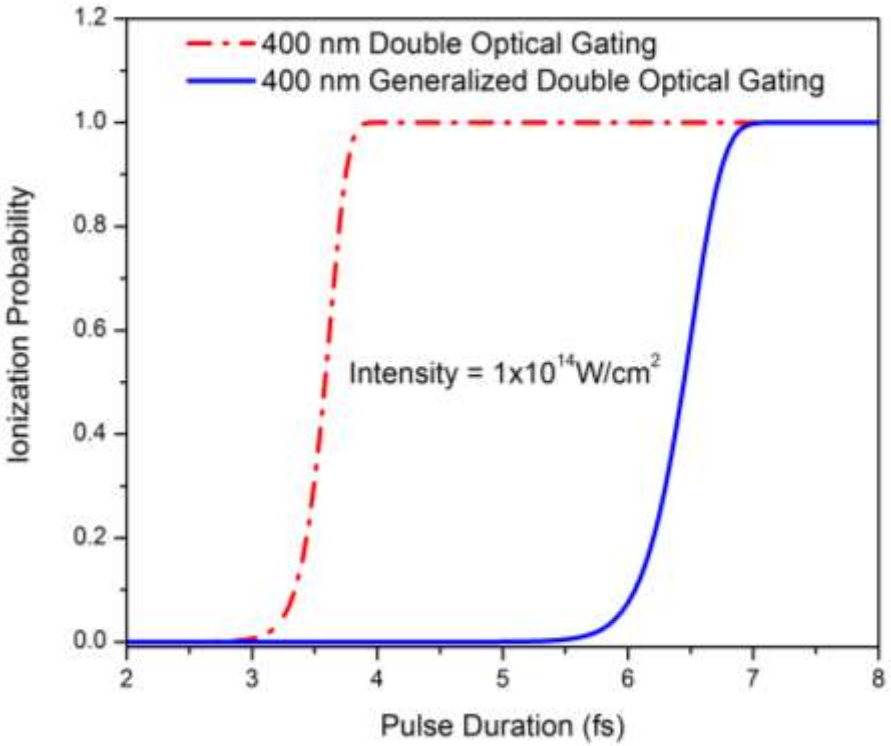

Figure 2-12 Comparison of ground state depletion as a function of pulse duration, from [24]

In conclusion, we can see that a 400 *nm* driving pulse comprised of about five optical cycles can produce single attosecond pulse using GDOG technique without completely depleting the ground state. The required delay time is 6.9 *fs*, which is comparable to the driving laser pulse duration of 6.5 *fs*. This is desirable to maintain a high laser intensity inside the gate. Also, sub 10 *fs* 400 *nm* pulses have been generated by pulse compression through self phase modulation in gas filled hollow core fiber [31] [32][33]. So GDOG is promising for generating isolated single attosecond pulses from 400 *nm* driving lasers.

To implement GDOG to generate single attosecond pulses, a driving laser with pulse duration of around 7 *fs* is required. However, the 400nm pulses from a BBO crystal is 35 *fs*, we need to compress them to be shorter. In the next chapter, I will discuss how we generate 400nm sub-10 *fs* short pulses.

Chapter 3 - Towards Intense Single Attosecond Pulses Generation

From the previous chapter we know that in order to generate isolated single attosecond pulses with 400 *nm* driving lasers, a 6.5 *fs* 400 *nm* driving laser is required. In order to generate such a short pulse, we use a noble gas filled hollow core fiber[34] and compensate the chirp using chirped mirrors.

3.1 400 *nm* short pulse generation

The spectral broadening of the pulse is caused by self phase modulation (SPM). SPM [35] is the process that, for an ultrashort laser pulse, when travelling in a nonlinear medium, it will produce a phase shift in the pulse due to the intensity dependent index of refraction which change the pulse's spectrum. The change of refractive index with intensity is known as the optical Kerr effect, and can be expressed as

$$n = n_0 + n_2 I(\mathrm{t}) \tag{3.1}$$

Here $I(t)$ $[W/cm^2]$ is the laser intensity, n_0 is the linear refract index of the medium, and n_2 $[cm^2/W]$ is the second order nonlinear refractive index of the medium.

The intensity of a Gaussian beam at a particular longitudinal position z is given by [23]:

$$I(r) = I_0 \exp\left[-2\frac{r^2}{w^2}\right] \tag{3.2}$$

so at different radial positions the intensity is different. This leads to a spatial variation of the index of refraction. The index of refraction is larger at the center of the beam than at the edges. This is very similar to the case when a laser pulse goes through a positive lens.

When the pulse goes through a nonlinear medium of length L, a nonlinear phase is added, and the phase shift is given by:

$$\Delta\varphi_{nl} = \frac{2\pi}{\lambda_0} n_2 I(t) L \tag{3.3}$$

The total phase is

$$\varphi = \frac{2\pi}{\lambda_0}[n_0 + n_2 I(t)]L \tag{3.4}$$

Frequency is the time derivative of a phase, so we can get

$$\omega(t) = \frac{d\varphi}{dt} = \omega_0 + \frac{2\pi}{\lambda_0} n_2 L \frac{dI(t)}{dt} \tag{3.5}$$

For a given frequency and medium, n_2 is a constant. We can see that the time dependent frequency produces new frequency components and thus enables the spectral broadening of the input pulse. Also, a positive chirp is introduced into the pulse, when we compensate the positive chirp after the fiber, we can then generate short pulses. Using a noble gas filled hollow core fiber is a good way to generate high energy (mJ) short pulses.

The experimental setup of our gas filled hollow core fiber is shown in the following figure. The hollow core fiber is 70 *cm* long, the inner and outer diameters of the fiber are 400 μm and 6 *mm*. The fiber is fixed inside a stainless steel tube. On each end of the tube, a 400 *nm* AR coated window (1 *mm* thickness) is attached. We fill the tube with neon gas, and the pressure within the tube can be controlled up to 30 *psi*. The whole setup is mounted on two translational stages. Each of the translation stages includes a linear stage (Newport UMR8.25) and a vertical Z stage (OptoSigma 122-0150), this allows us to tune the hollow core fiber in both vertical and horizontal directions perpendicular to the direction of the laser transmission

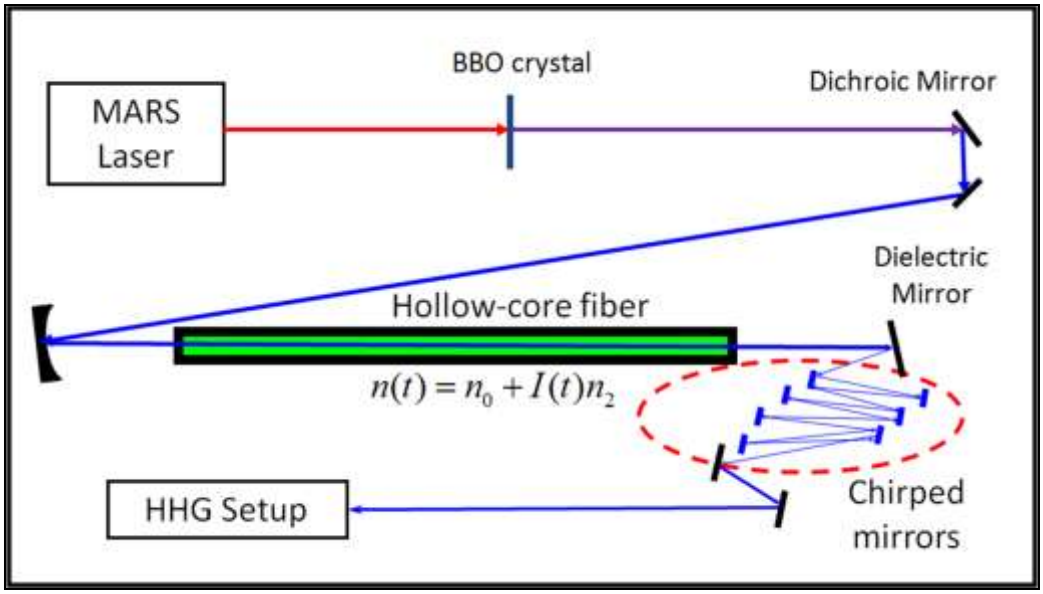

Figure 3-1 400 *nm* short pulses hollow core fiber setup

The 400 *nm* laser pulse is focused into the chamber with a 1.5m focal length aluminum coated mirror. The focal point is at the entrance of the fiber. After the hollow core fiber, the beam is collimated with a 2m focal length aluminum mirror. The positive chirp of the 400 *nm* pulses introduced by self phase modulation and material dispersion is compensated using chirped mirrors (UltraFast Innovations, CM82). The bandwidth of the chirped mirrors is from 350 *nm* to 450 *nm*. With 0° incident angle, the group delay dispersion of each mirror is -50fs^2. There are 8 such chirped mirrors in total, giving a total negative dispersion of -400 fs^2. The collimated beam is then sent into the chirped mirror set. The dispersion and reflection curve of the mirrors are shown in the figure below. The extra negative chirp can be compensated by a set of compensation plates (fused silica) in order to generate as short pulses as possible.

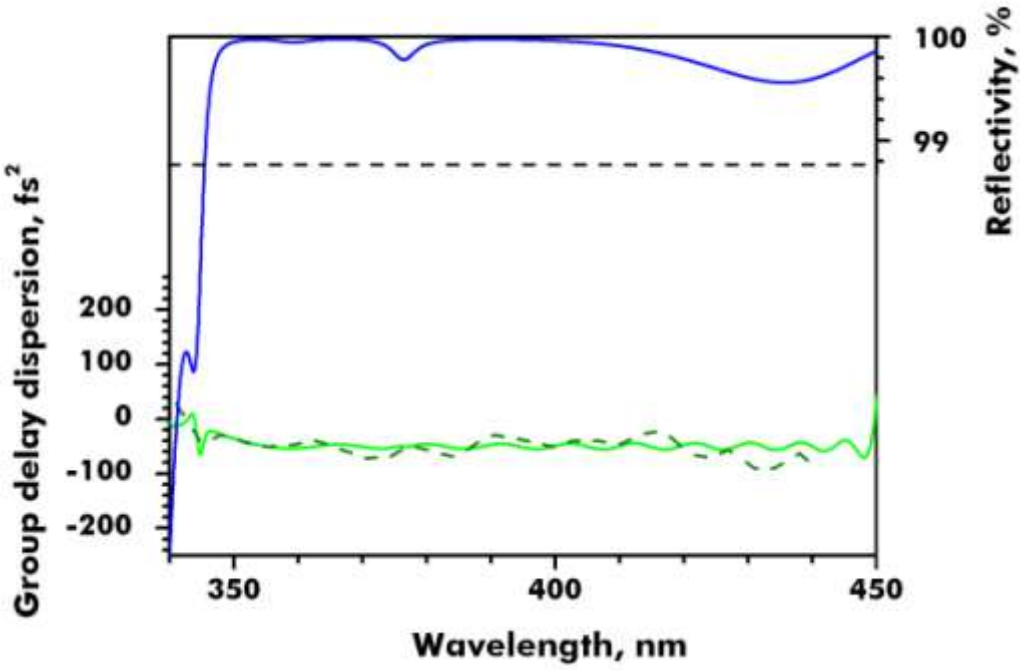

Figure 3-2 Chirped mirror reflectivity and GDD curve

We optimized the output beam by carefully aligning the fiber and scanning the neon gas pressure inside the chamber. By carefully tuning the fiber, we can get an output coupling efficiency of 75% in vacuum and 55% with 30 *psi* neon gas. The output beam profile is shown below.

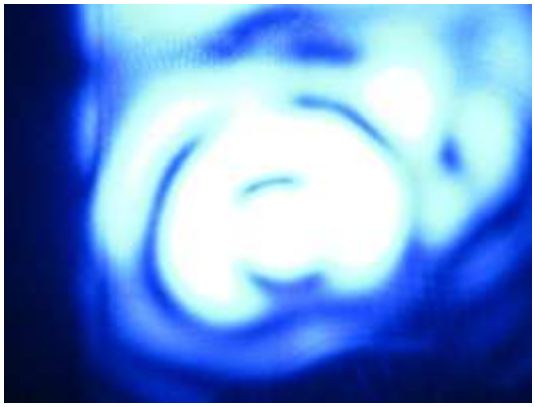

Figure 3-3 Beam profile of 400 *nm* pulses after the hollow core fiber

The hollow core fiber chamber is first vacuum pumped and then filled with neon gas. The following figure shows the fiber output spectrum with 0 *psi*, 10 *psi*, 20 *psi*, 30 *psi* neon gas.

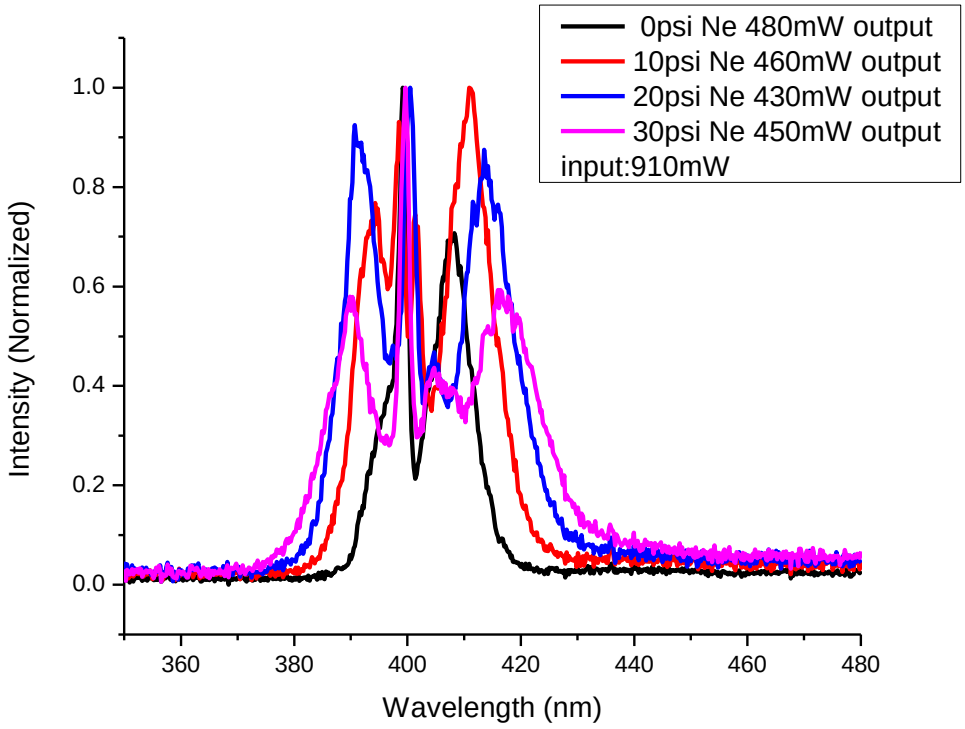

Figure 3-4 The hollow core fiber output pulse spectrum at different Neon gas pressure.

With 1.2 *mJ* 400 *nm* input laser pulse, the output pulse is ~650 *mJ*. The output pulse spectrum is as followed.

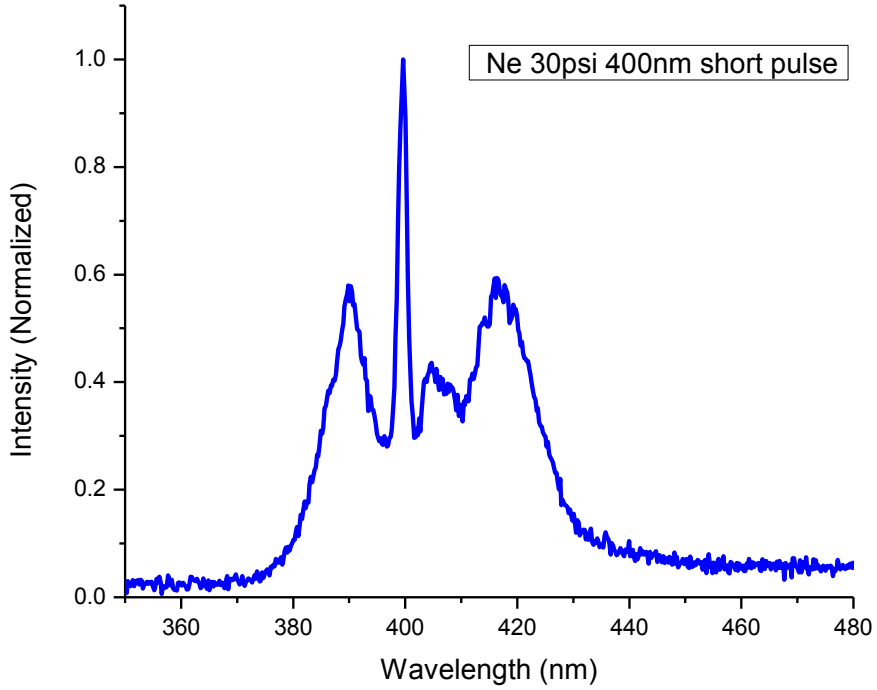

Figure 3-5 400 *nm* short pulses spectrum after chirped mirrors. The bandwidth is 37 *nm*, which corresponds to 6.5 *fs* transform limited pulse. The hollow core fiber is filled with 30 *psi* neon gas.

We achieved a bandwidth of 37*nm*, corresponding to a 6.5 *fs* transform limited pulse. The pulse energy after the chirped mirrors was around 0.5 *mJ*.

Another Approach to Generate 400 *nm* short pulses

Here we describe another approach to generate 400 *nm* short pulses. First we generate 800 *nm* short pulses using hollow core fiber and compress them with chirped mirrors. Next a BBO crystal is then placed after the chirped mirrors to generate broadband 400 *nm* short pulses. The experiment setup is shown below.

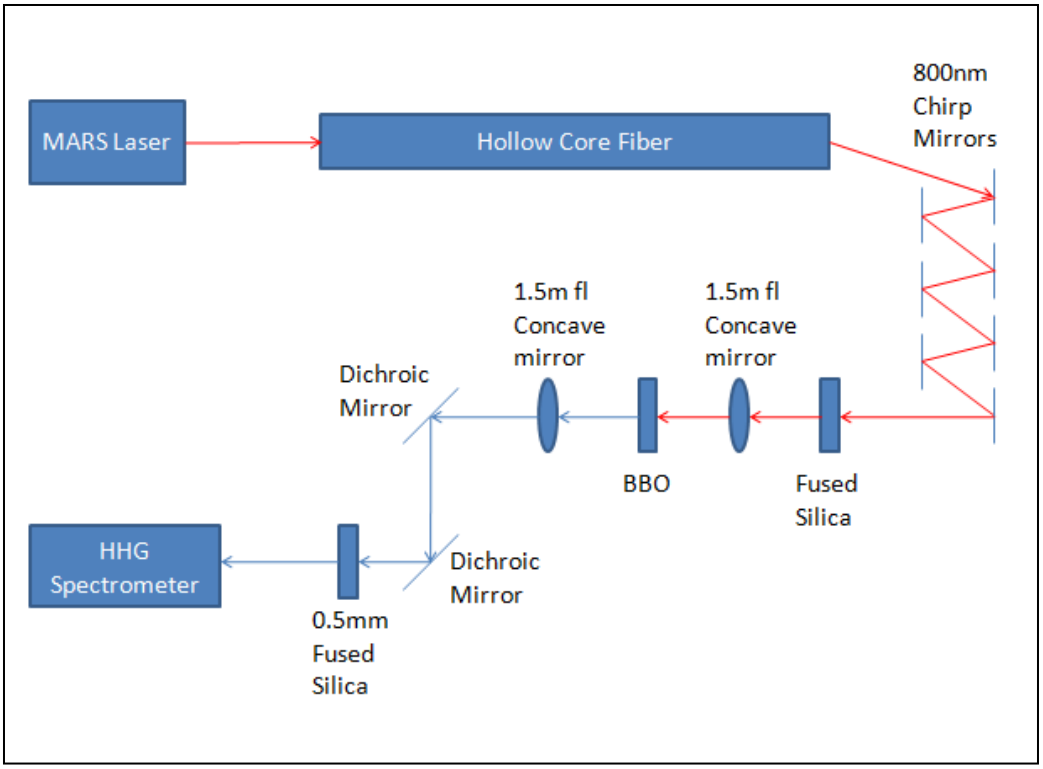

Figure 3-6 Experimental setup for an alternative method to generate 400 nm short pulses

The 800 *nm* 35 *fs* laser pulses were focused into a 900 *mm* long hollow core fiber by a 1.5 *m* focal length focus mirror. The inner diameter was 400 μm and the outer diameter was 6 *mm*. After the chirped mirrors, a 1.5 *m* focal length concave mirror was used to focus the beam into the BBO to increase the laser intensity on the BBO so as to increase the second harmonic generation efficiency. In this experiment, we tried 10 μm, 50 μm, 141 μm, 300 μm thickness BBO crystals. The measured 400 *nm* short pulse spectra with different BBO crystal thickness are shown in the figures below.

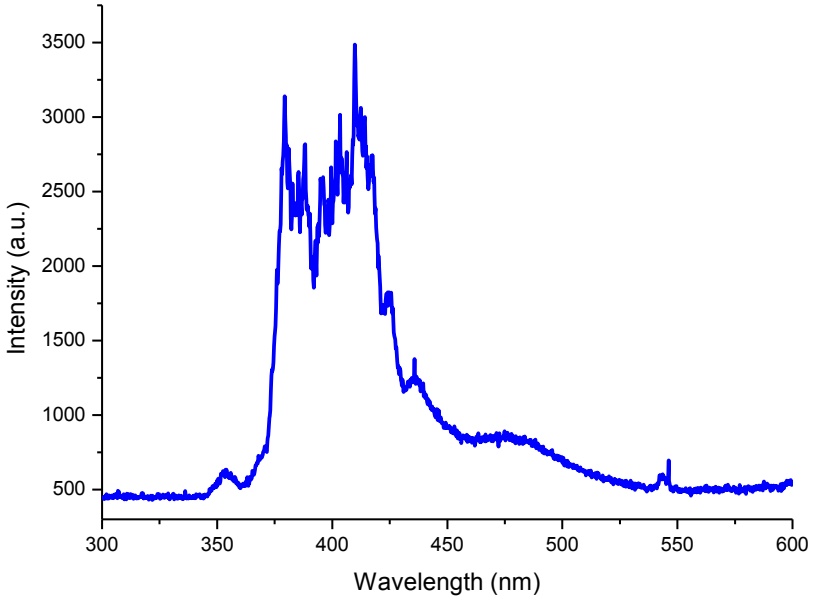

Figure 3-7 A 10 μm BBO crystal. The bandwidth is 46.7 *nm*, corresponding to a 5.2 *fs* transform limited pulse

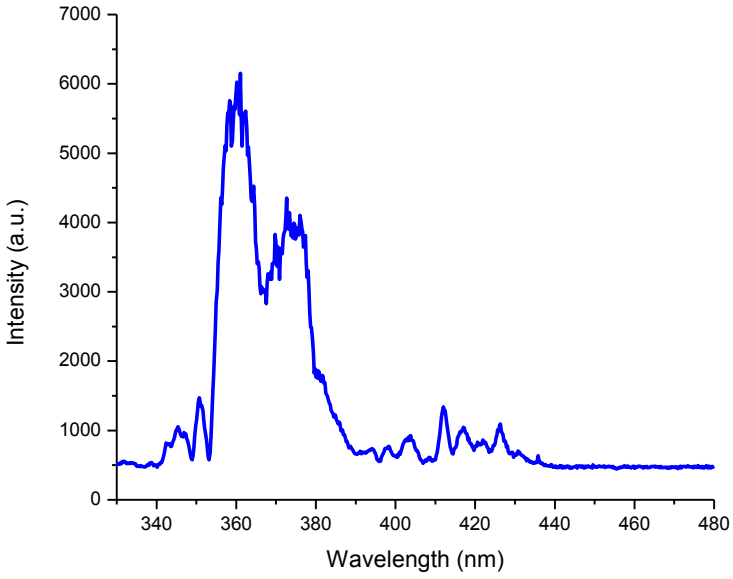

Figure 3-8 A 50 μm BBO crystal. The bandwidth is 23.5 *nm*, corresponding to a 10 *fs* transform limited pulse

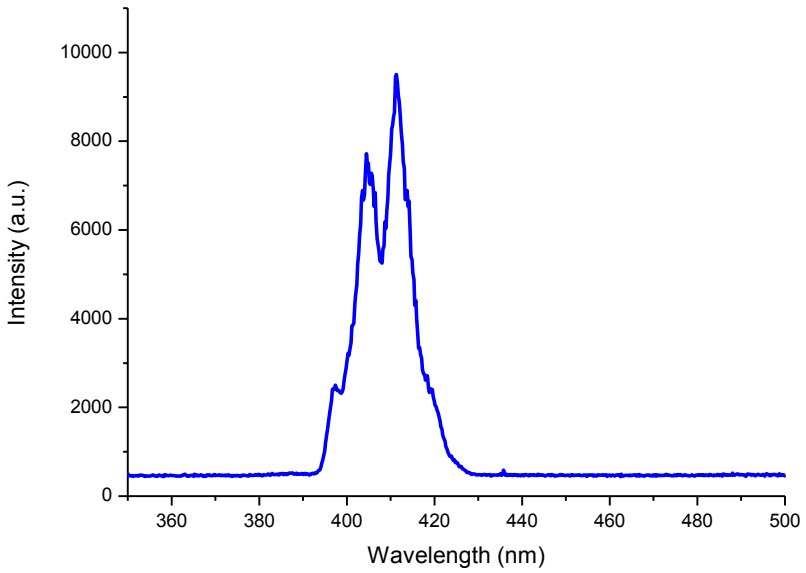

Figure 3-9 A 141 μm BBO crystal. The bandwidth is 20.4 *nm*, corresponding to a 11.5 *fs* transform limited pulse

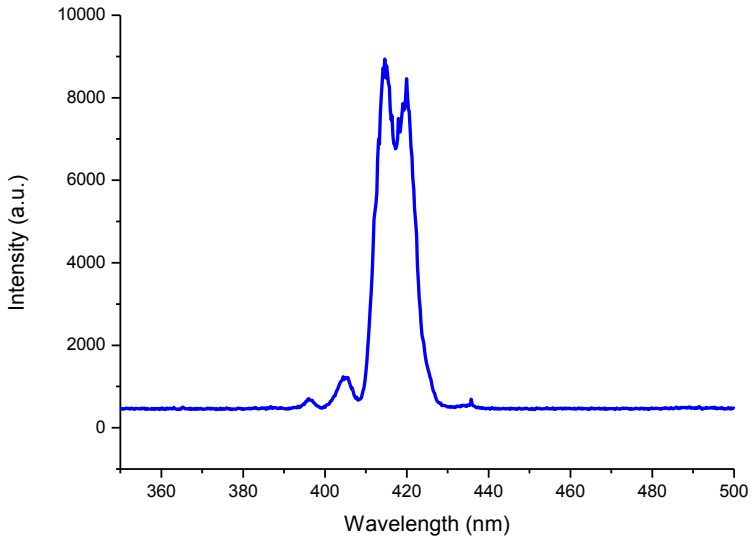

Figure 3-10 A 300 μm BBO crystal. The bandwidth is 10.8 *nm*, corresponding to a 21.8 *fs* transform limited pulse

As we increase the BBO crystal thickness, the generated SHG pulse's spectrum decreases, and the SHG power increases. However, the conversion efficiency is very low, as we need bandwidth of around 30 *nm* where the SHG conversion efficiency is around 1%. As this is too low for applications, we do not use this approach to generate 400 *nm* short pulse. We stick to generating 400 *nm* short pulse with 400 *nm* hollow core fiber and chirped mirrors.

The compressed 400 *nm* short pulses are focused into an argon gas target to generate high harmonics. The experimental setup is the same one as discussed in Chapter 2. The experiment result is shown in the figure below.

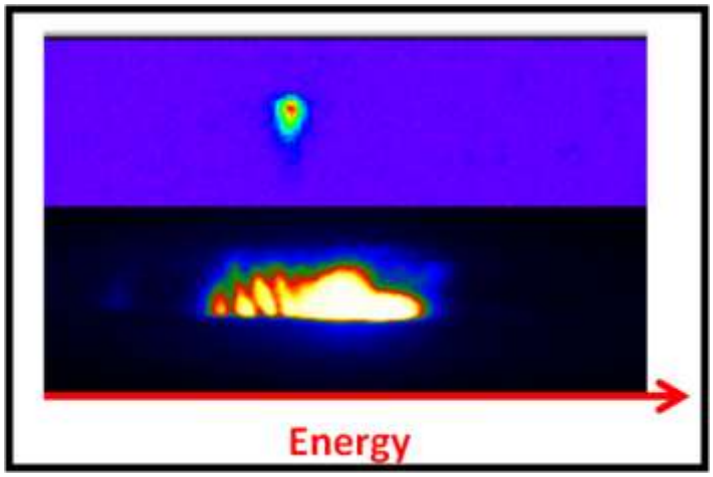

Figure 3-11 Spectrum of the 9th order high harmonic from 400 *nm* 35 *fs* long pulse (top one) and spectrum of the 9th order high harmonic from 400 *nm* sub-10 *fs* short pulse (bottom one).

We know that as we decrease the driving laser pulse duration, we expect the high harmonic spectrum to become wider. And this is what we observed. As can been seen from the experiment result in the figure above, when the driving pulse duration decreases, the high harmonic spectrum gets broadened.

3.2 400 *nm* short pulse characterization with SD-FROG

To measure the pulse duration of the 400 *nm* short pulse we generated through hollow core fiber, we implemented the self diffraction frequency resolved optical gating (SD-FROG) method. Since for 400 *nm* pulses, it is difficult to use SHG FROG, which is used in the KLS laboratory to measure 800 *nm* short pulses duration.

The 400 *nm* short incoming pulse was split into two replicas using a thin pellicle beamsplitter. The reflected beam was sent to a flat aluminum mirror which is perpendicular to the beam, and the transmitted beam was sent to a delay stage to introduce a time delay. The two replicas were then directed to a 1.5 *m* focal length concave aluminum mirror and focused into a 125 μm glass plate. The self diffraction signal was then isolated using an aperture and focused into the spectrometer with a lens. The diagram of SD-FROG is shown in the figure below.

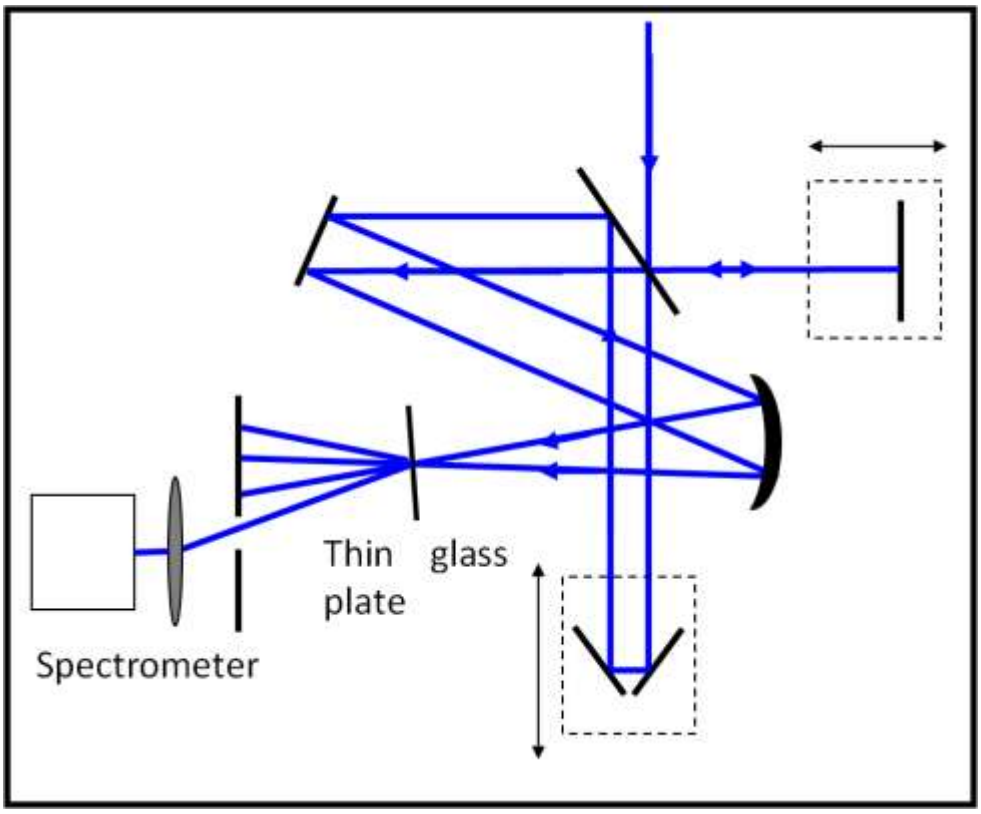

Figure 3-12 SD-FROG setup

For SD-FROG, the two laser pulses are spatially and temporally overlap at an angle in a nonlinear medium, and the two beams will interfere constructively and destructively creating a periodic structure of intensity.

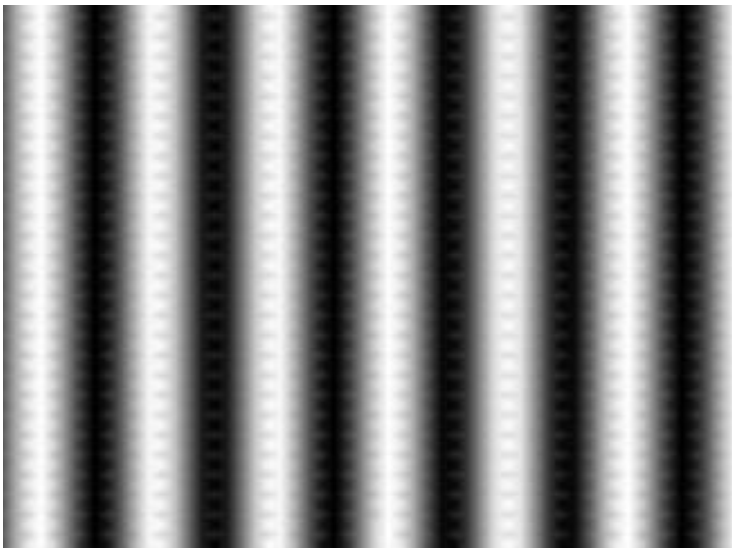

Figure 3-13 Intensity periodic variation

For a nonlinear medium, we know that

$$n = n_0 + n_2 I(\mathrm{t}) \tag{3.6}$$

As seen above the variation of intensity creates a transient nonlinear refractive index grating. The grating will diffract both beams, and self diffraction signal is produced.

According to the Newport company, overlapping the beam in time and space using the self-diffraction signal is extremely difficult, and they recommend that one should first build a SHG FROG as a starting point [36]. We developed another way to overlap the two beams. We first find the focal position of the focus mirror and place a CCD camera there. By tuning the mirrors we make sure two beam are spatially overlapped. Then we scan one of the delay stages to a position where we can see strong spatial interference, shown as the following figure. We can determine that this is where two beams are spatially and temporally overlapped.

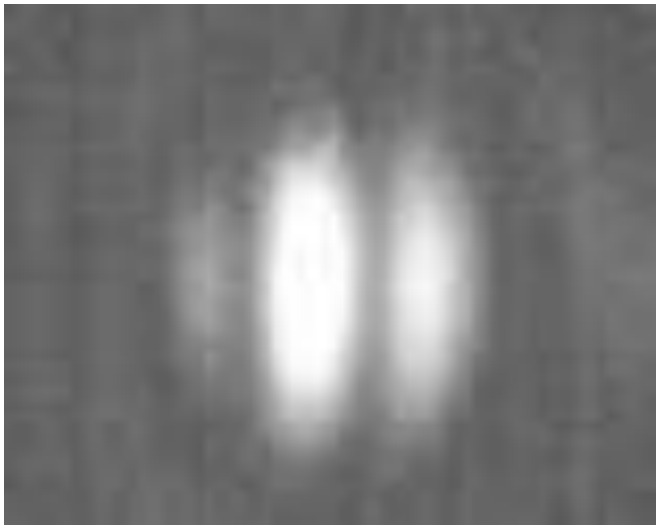

Figure 3-14 Time and space overlap of the two beams

Later we put the 100 μm thick quartz plate back, and we could see the diffracted beam, show in the figure below.

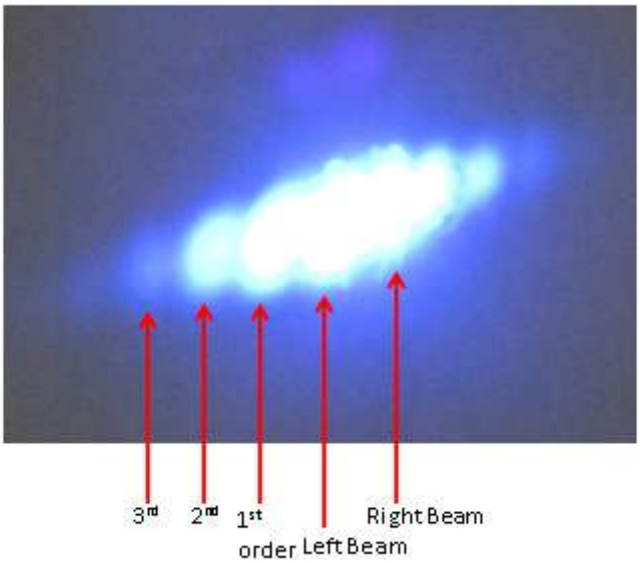

Figure 3-15 The self diffraction pattern

To minimize the pulse duration measurement error, the crystal should be thin and the crossing angle should be small. [37] The spectrogram of the self-diffraction signal can be expressed by the following equation:

$$I_{SD}(\omega,\tau) \propto \left| \int (E(t) + E(t-\tau)) e^{-i\omega t} dt \right|^2 \tag{3.7}$$

Because of the recent technical problems of the MARS laser, we have been unable to continue to use the SD-FROG to measure the 400 *nm* short pulse duration. We can only estimate the pulse duration from the corresponding spectrum. Once the MARS laser is repaired, we can use the SD-FROG to measure the short pulse duration.

3.3 400 *nm* GDOG

We designed the Generalized Double Optical Gating (GDOG) for 400 *nm* driving pulse. In the traditional GDOG setup, a weak second harmonic is added to the fundamental, shown in the figure below

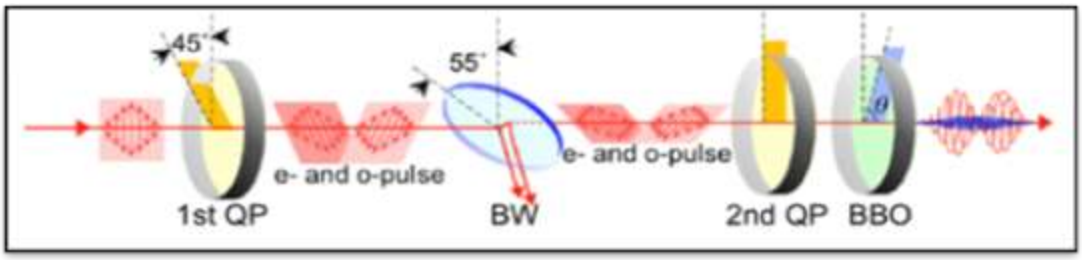

Figure 3-16 GDOG setup (From [20])

In the GDOG for 400 *nm* driving pulsse, it is not possible to add a second harmonic to the fundamental 400 *nm* pulse. We instead superimpose two counter rotating elliptically polarized 400 *nm* pulses and add a weak linearly polarized 800 *nm* pulse as the gating. We are still working on the 400 *nm* GDOG scheme, we will try to realize it in the future. In the next chapter, I will discuss the applications of attosecond pulses

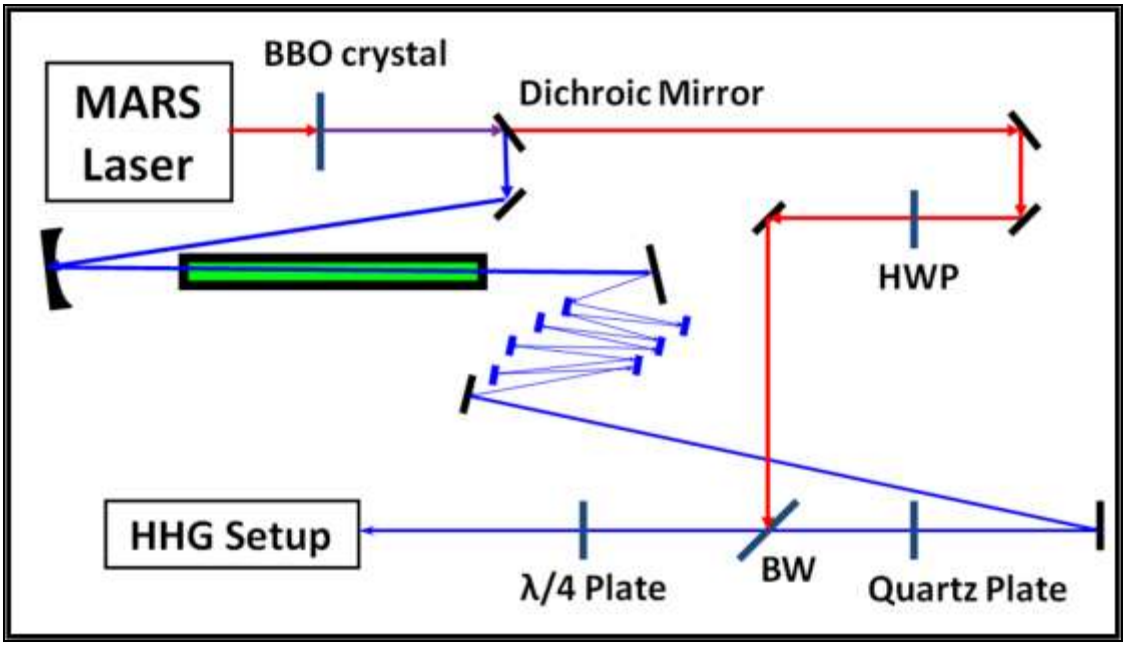

Figure 3-17 400 *nm* GDOG setup, the 400 *nm* short pulse after the hollow core fiber and chirped mirrors goes through a quartz plate, a Brewster window and a quarter wave plate. The 800 *nm* laser goes through the dichroic mirror and its polarization will be changed 90° with a half wave plate, it recombines with 400 *nm* pulses at the Brewster window.

.

Chapter 4 - Attosecond Pulse Applications

One important application of attosecond pulse is to perform pump-probe experiments to study the dynamics of electron-electron correlation with attosecond precision, such as the autoionization process. In this chapter, the autoionization of argon atoms is studied by transient absorption spectroscopy with isolated attosecond pulse.

The Fano profile is the signature of the autoionization process, it is a result of interference between the direct ionization and the decay from an autoionization state due to configuration interaction[38].

For this chapter, Dr. He Wang and Michael Chini conducted most of the experiments and data analysis [39], my contribution to the work was to analyze the spectrometer resolution, which is also the main point of this chapter.

4.1 Introduction and Experimental Setup

The absorption cross section of an autoionization state can be described by the Fano formula

$$\sigma = \sigma_a \frac{(q+\varepsilon)^2}{1+\varepsilon^2} + \sigma_b \tag{4.1}$$

Where σ_a and σ_b are the cross section of continuum state that interacts and does not interact with autoionization state respectively, q is a parameter which determines the shape of the resonance and $\varepsilon = \frac{E - E_r}{\Gamma/2}$ is the reduced energy, E_r is the resonance energy, Γ is the natural width of the resonance. The argon cross section is plotted in the figure below

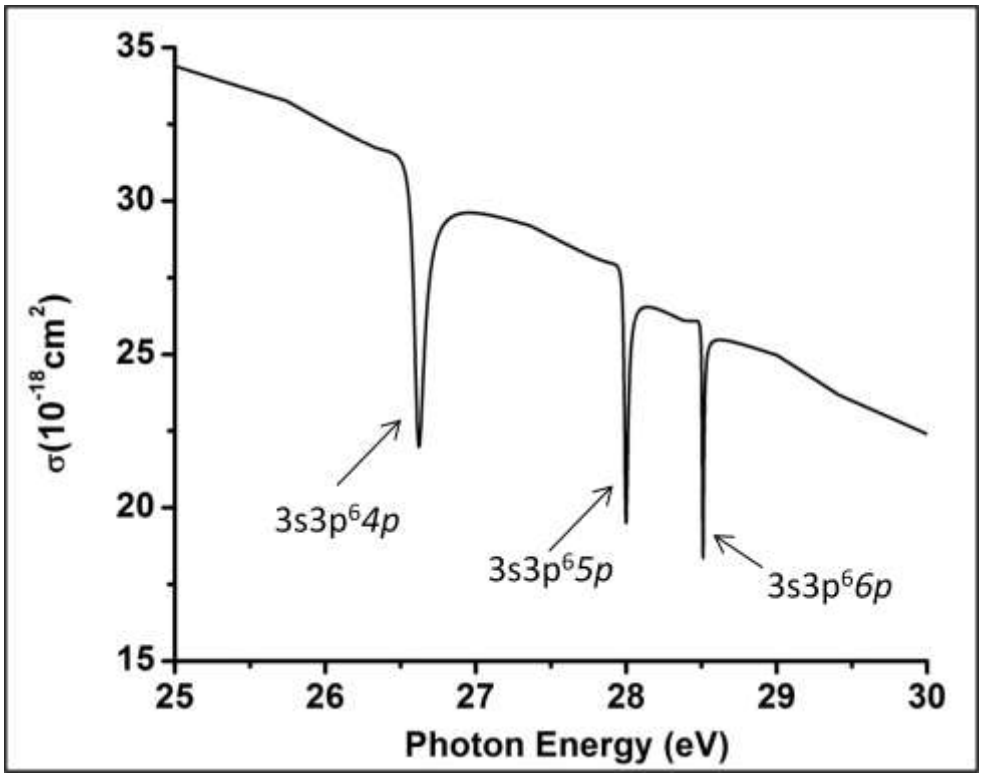

Figure 4-1 Argon cross section between 25eV and 30eV

The width of each autoionization resonance peak is shown in the table below.

State	Γ(meV)
$3s3p^6 4p$	80
$3s3p^6 5p$	28.2
$3s3p^6 6p$	12.6

Table 4-1 FWHM for the first three autoionization resonance peaks of argon

When XUV pulses go through the argon gas target, some of the energy will be absorbed. The transmitted spectrum can be written as

$$T(\omega) = \exp[-\rho\sigma(\omega)L] \tag{4.2}$$

Here ρ is the argon gas target density, $\sigma(\omega)$ is the argon gas cross section, L is the length of the gas target. The transmitted XUV spectrum is plotted in the figure below.

Attention needs to be paid to the resolution of the XUV spectrometer, which is very important in this experiment.

The measured data is the convolution of the spectrum and an experimentally determined instrumental function $F(E)$, that is $\sigma^{\exp}(E) = \sigma(E) * F(E)$, here we assume the instrumental function $F(E)$ is a Gaussian function.

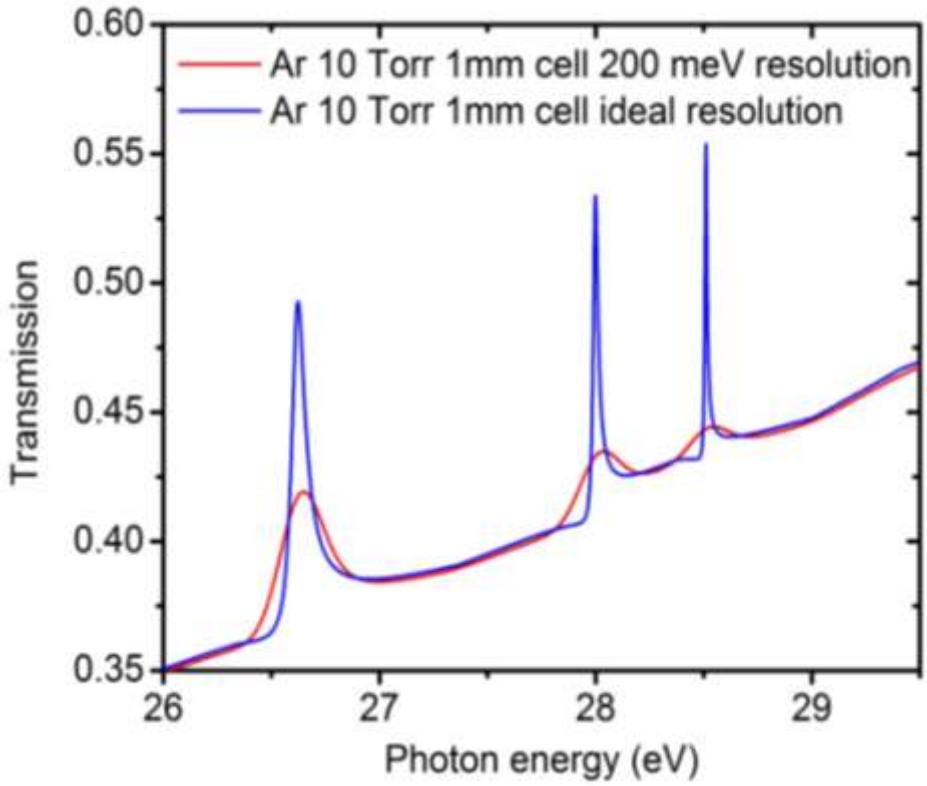

Figure 4-2 Transmitted XUV spectrum with different spectrometer resolution. Blue curve: ideal spectrometer resolution, Red curve: 200 *meV* resolution

Following is the experiment setup.

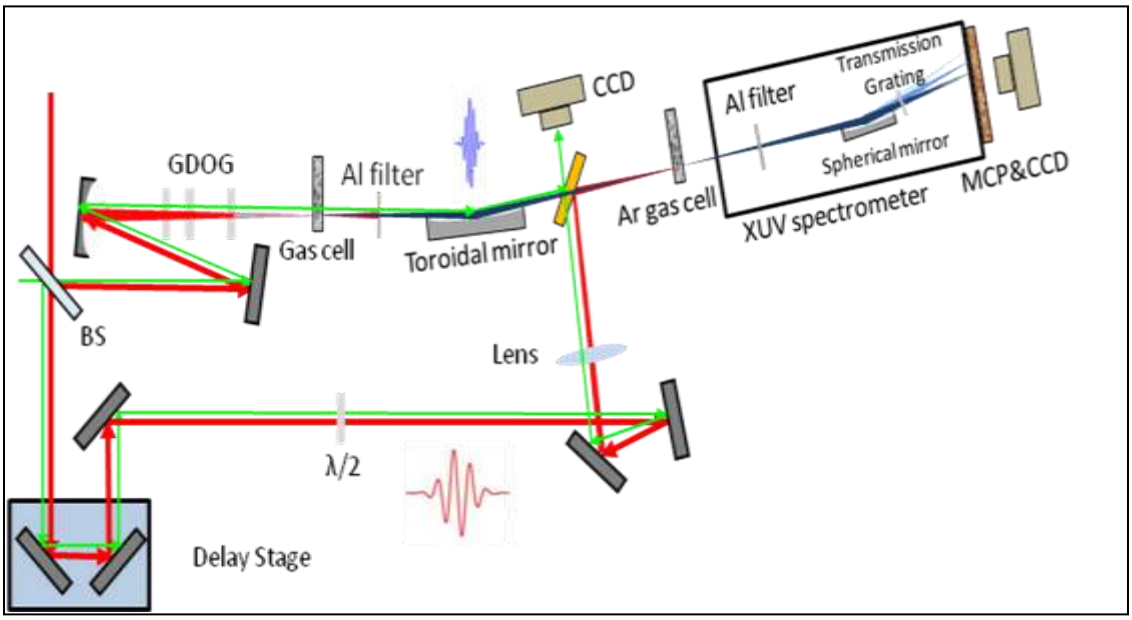

Figure 4-3 Attosecond transient absorption experimental setup. The 7 *fs* pulse was split into two by a 50/50 beam splitter (BS). Half of the NIR beam propagated through the GDOG optics (QP1, BW, QP2, BBO) and was focused onto the argon gas cell (GC1) to generate the single attosecond pulses. After the XUV beam passed through the aluminum filter (F), it was focused by a toroidal mirror (TM) into the second gas cell (GC2) filled with argon gas as the absorption target. The other half of the NIR beam was delayed by a PZT mirror and then focused by a lens (L) and recombined with XUV beam by a hole mirror (HM). The transmitted XUV was refocused by a spherical mirror (SM) and dispersed by a transmission grating (TG) onto an MCP/Phosphor and CCD image recorder. From [40]

The femtosecond laser pulses are from the MARS laser system as discussed in Chapter 2, with a carrier envelope phase stabilized Ti:sapphire regenerative amplifier (Coherent Legend Elite Duo). The laser pulse is 2.5 *mJ*, 1 *kHz* repetition rate with a central wavelength of 800 *nm*. The pulse was focused into a 400 μm inner diameter hollow core fiber filled with neon gas. After being compressed by chirped mirrors, we were able to get 1 *mJ* 8 *fs* near-infrared (NIR) pulses centered at 750*nm*.

The beam was then split into two parts with a broadband 50:50 beam splitter where half of the beam produces single attosecond pulses using the generalized double optical

gating (GDOG) from argon gas. The attosecond XUV beam passed through a 300 *nm* aluminum filter and then was focused by a toroidal mirror (*f*=250 *mm*, 9.6 degree grazing incidence angle, R=90.5 *mm*, r=3230 *mm*, ARW Optical Corporation). The focal point was at the second gas cell. The second gas cell was filled with 25 *Torr* argon gas. The other half of the NIR beam was recombined collinearly with the XUV attosecond pulses at the second gas cell. A piezo electric transducer (P-752.1 CD PI) was used to introduce delay between the NIR and XUV pulses. The transmitted XUV pulses were refocused using a spherical mirror, and its spectrum was recorded using a XUV spectrometer. Another aluminum filter was installed before the XUV spectrometer to block the residue IR pulses.

The spectrometer consists of a gold-coated spherical mirror (2 degree grazing incidence angle), a 2000 lines/mm transmission grating, a MCP with phosphor screen and a CCD camera. The layout of the spectrometer is shown in the figure below. The focal length of the spherical mirror is 50.8 *cm*, and it is positioned 94 *cm* after the second argon gas cell. The spherical mirror is used to focus the dispersed XUV to the MCP, which is 106 *cm* after the mirror, as shown in the graph below. The spherical mirror is mounted at the incident angle of 88°. The grating is positioned 5 *cm* after the toroidal mirror.

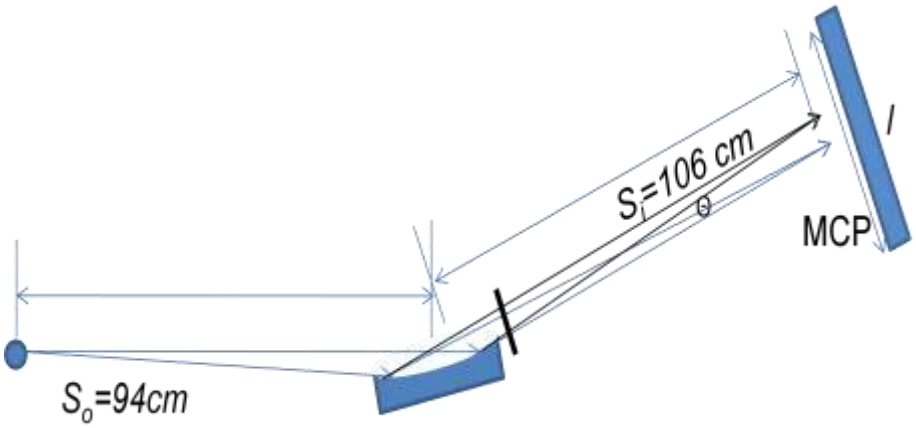

Figure 4-4 XUV spectrometer layout

4.2 Resolution of the spectrometer

The resolution of the spectrometer is determined by the spot size of the XUV pulses, the resolution of the grating, the resolution of the MCP and phosphor, and the resolution of the CCD camera. We need to analyze the resolution limit of each of these factors, and from there we can determine the resolution of the whole system.

The XUV pulse Spot size

The focal point in the second argon gas cell serves as the entrance slit to the spectrometer, so the focal spot size of the XUV beam at the argon gas cell position is a factor that can determine the resolution of the spectrometer. The laser spot size in the argon gas cell is less than 50 μm, so the spot size on the MCP surface should be less than $\frac{S_i}{S_o} \times 50\mu m = 56.4\mu m$.

Grating

The transmission grating use has a groove density of 2000 lines/mm. The reciprocal linear dispersion of the grating is given by

$$\frac{d\lambda}{dl} = \frac{d\cos\alpha}{r}$$

Where α is the diffraction angle, r is the distance from the transmission grating to the MCP detector which is 106 *cm, d* is the grating period. Here we only consider the first order diffraction. For first order diffraction,

$$\frac{d\lambda}{dl} = 0.47nm/mm$$

this corresponds to the energy dispersion

$$\frac{dE}{dl} = 0.5229E^2(eV/m) = 0.32eV/mm$$, when E=27 *eV*.

Resolution of the MCP and Phosphor

The distance between the MCP and the phosphor is 1 *mm*. Because of the distance, electrons from the MCP channels will be dispersed. The maximum energy electrons have at the exit of the channel is 20 *eV*, this corresponds to a velocity of $2.65\times10^6 m/s$. So the maximum velocity parallel to the phosphor is $2.65\times10^6 m/s$. Assuming the initial

perpendicular velocity is zero at the exit, we can estimate the time period within which electrons arrived at the phosphor is $2.7\times10^{-11}s$, so the spatial resolution of the MCP and phosphor is 100-200μm.

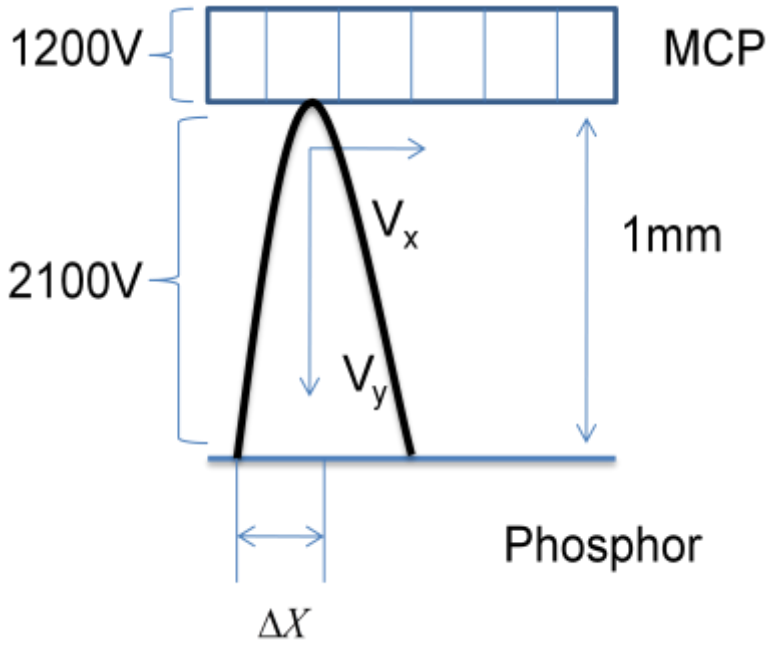

Figure 4-5 Electrons from the MCP channels will get dispersed when they reach the phosphor

Resolution of the CCD Camera

The 1024×1024 pixel CCD camera is thermoelectrically cooled to -60. Using a pair of lens, the CCD camera was focused on an area of $\sim 2cm\times 2cm$. So the resolution on the CCD camera was $19\mu m/pixel$. We need 3~4 pixels to describe a peak, so the resolution on the CCD camera is around 80 μm.

Conclusion

From the above analysis, we can see that in our spectrometer, the limiting factor of the resolution is the MCP, and it is around 100μm. In experiments we can see MCP quantum noise occupy 2~4 pixels of CCD camera, and this supports our conclusion. The 100-200μm resolution corresponds to the energy resolution of 30-60meV. It is estimated that the best resolution will be 30-60 *meV*.

In the following figure, the transmitted XUV spectrum is measured.

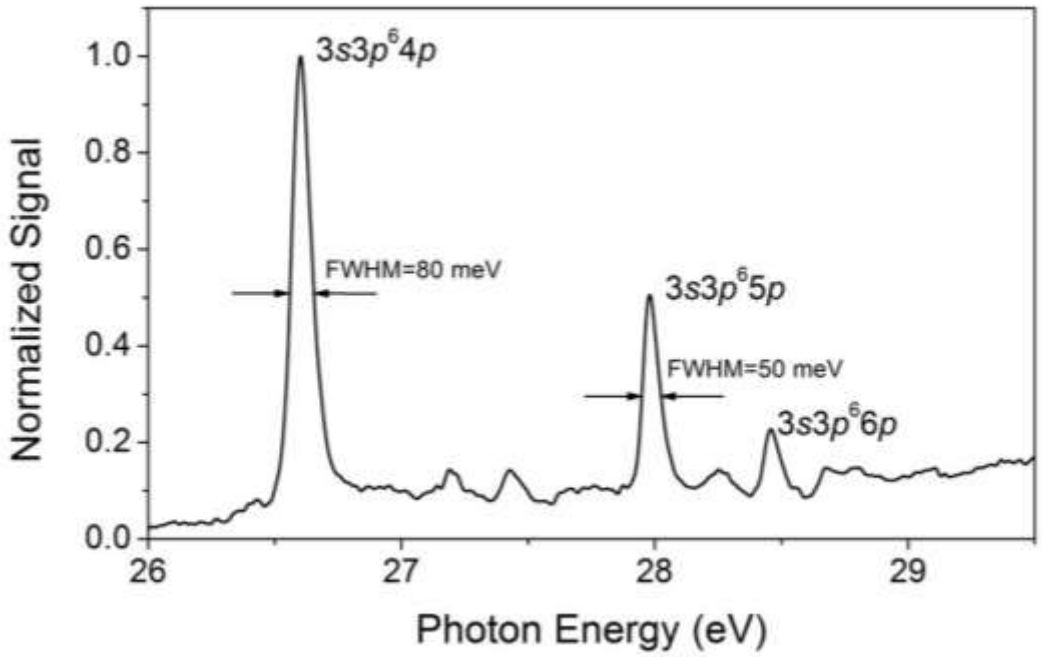

Figure 4-6 Experimentally measured transmitted XUV spectrum of the Argon $3s3p^6np^1P$ autoionization state

We compare the experiment result with the convolution result, show as in the figure below

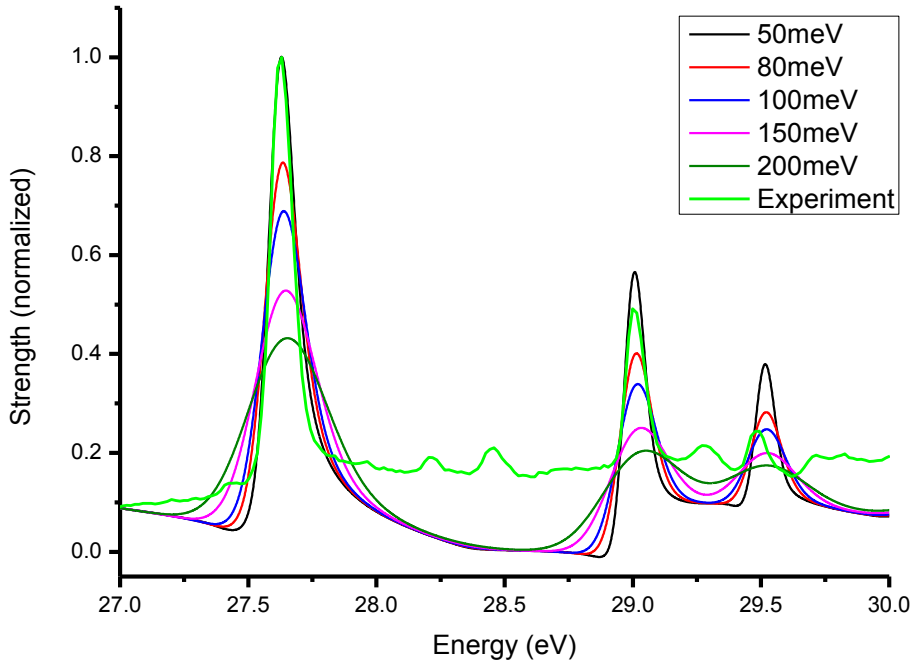

Figure 4-7 Comparison among convolution results with experimental results.

From the calibration we can see that 50 *meV* resolution matches experiment result best, so the energy resolution in the experiment is around 50 *meV*.

The following two figures are experiments results conducted mainly by He Wang and Michael Chini, and are included here for completeness. The experimental results shows the transmitted XUV spectrum for different delays between the XUV pulses and the NIR pulses. Figure 4-8 shows the result of the transmitted XUV spectrum of argon gas in a NIR laser field of peak intensity 10^{11}W/cm^2. As the delay between the XUV pulses and the NIR pulses changes, we can observe shifting and splitting of the resonance peaks.

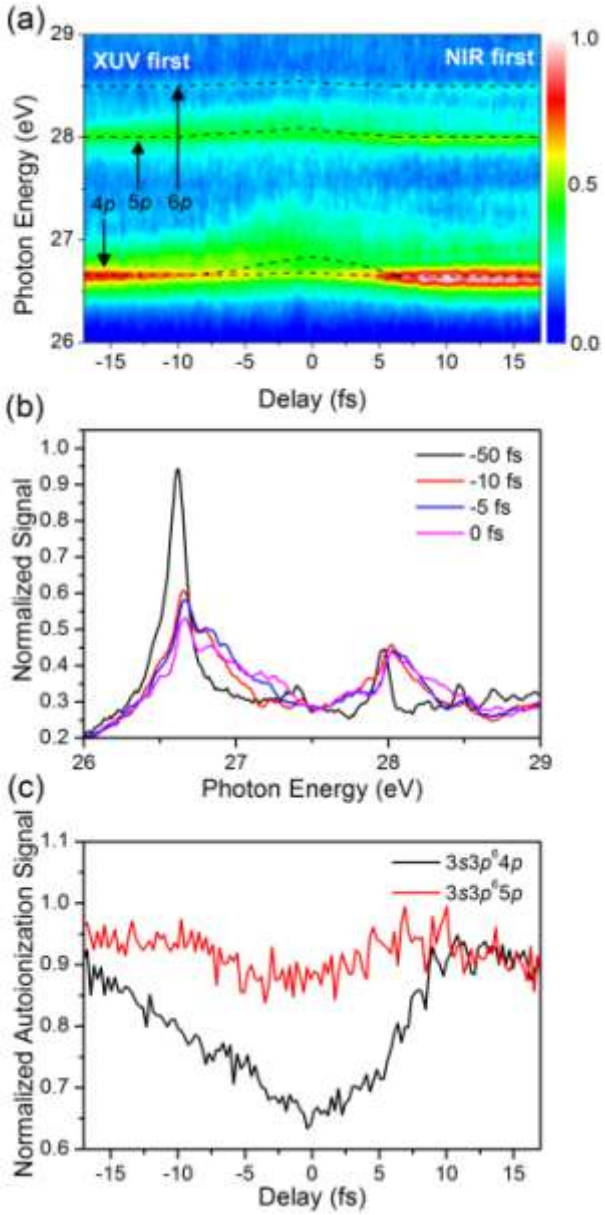

Figure 4-8 Transmitted attosecond XUV spectrum of argon in a strong NIR laser field with a peak intensity of ~10^{12} W/cm^2, From [41]

Figure 4-9 shows the result of the transmitted XUV spectrum of argon gas in a NIR laser field of peak intensity 10^{12} *W/cm*^{2}. As the delay between the XUV pulses and the NIR pulses changes, we can observe shifting and splitting of the resonance peaks. The NIR pulse is stronger than that in Figure 4-8, the shifting and the splitting of the resonance peaks is stronger.

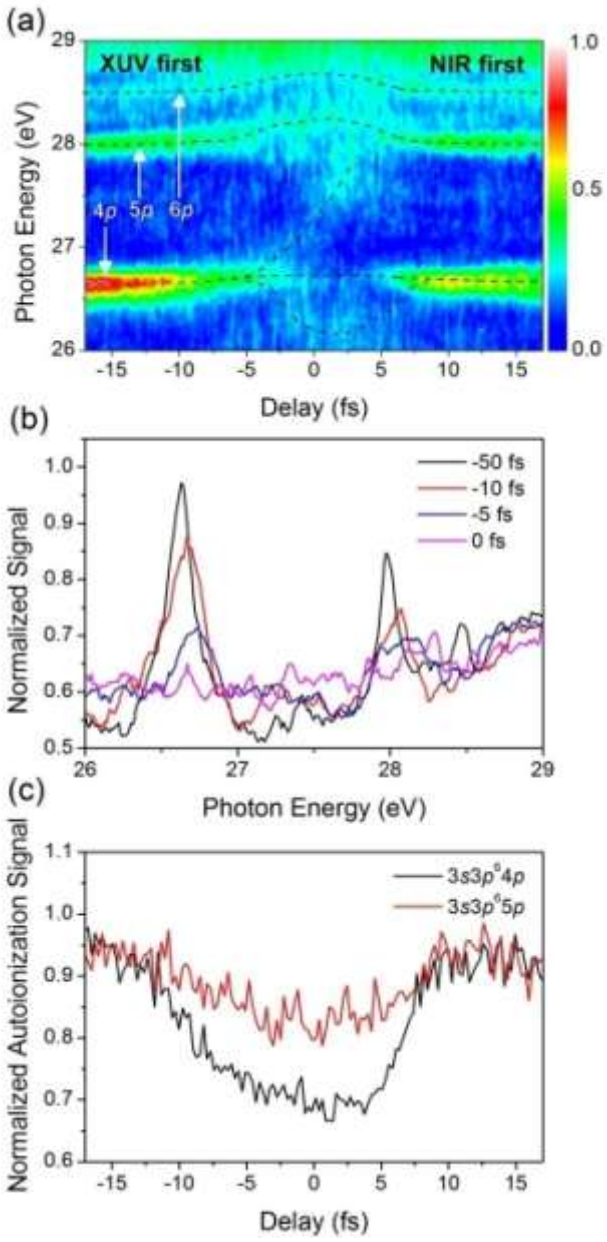

Figure 4-9 Transmitted attosecond XUV spectrum of argon in a strong NIR laser field with a peak intensity of ~10^{12} W/cm^2, from [41]

Chapter 5 - Conclusions and Future Work

In this thesis, a first step towards intense isolated single attosecond pulses generation is demonstrated. Here, 400 *nm* femtosecond laser pulses are used to generate high order harmonics since the HHG efficiency scales as λ^{-6} in the plateau region. We studied the dependence of high harmonic generation efficiency on the ellipticity of the 400 *nm* driving laser pulse and compared it with the ellipticity dependence of 800 *nm* driven high harmonics. It is found that 400 *nm* driven high harmonics yield drops slower as the driving pulse ellipticity increases than 800 *nm* driven high harmonics yield. A semi classical theory is developed to explain the ellipticity dependence of high harmonics. The model is based on the assumption that the major contribution to high harmonic generation comes from electron trajectories in which the transverse displacement is compensated by an initial electron transverse velocity. The theory is compared with experimental results and they match well. Next, a 400 *nm* short pulse with bandwidth of 37 *nm* is produced with hollow core fiber and chirped mirrors, this bandwidth corresponds to 6.5fs transform limited pulses. And we designed a revised version of Generalized Double Optical Gating (GDOG) method using 400 *nm* driving lasers to extract a single attosecond pulse.

For future work, we will try to realize the 400 *nm* GDOG scheme we proposed. First we will finish building the SD-FROG, which will enable us to measure the 400 *nm* sub-10fs short pulse duration. Then we will try polarization gating to see if we can see any high harmonic spectrum broadening effect. Next the proposed 400 *nm* generalized double optical gating scheme will be tried. There are still many challenges, for example, the pulse duration and stability of the 400 *nm* short pulse, the temporal and spatial overlap of 800 *nm* pulses and 400 *nm* pulses in the proposed GDOG scheme and other as yet unknown factors.

Publications

Journal Articles

1) **"Ellipticity dependence of 400 *nm*-driven high harmonic generation"**, Sabih D. Khan, **Yan Cheng**, Max Moller, Kun Zhao, Baozhen Zhao, Michael Chini, Gerhard. G. Paulus, and Zenghu Chang, Appl. Phys. Lett. 99, 161106 (2011)
2) **"Dependence of high harmonic generation yield on driving-laser ellipticity**", Max Moller, Sabih D. Khan, **Yan Cheng**, Kun Zhao, Baozhen Zhao, Michael Chini, Gerhard. G. Paulus, and Zenghu Chang, submitted
3) **"Sub-cycle AC Stark shift"**, Michael Chini, Baozhen Zhao, He Wang, **Yan Cheng**, S. X. Hu, and Zenghu Chang, submitted
4) **"Attosecond Time-Resolved Autoionization of Argon"**, He Wang, Michael Chini, Shouyuan Chen, Chang-Hua Zhang, Feng He, **Yan Cheng**, Yi Wu, Uwe Thumm, and Zenghu Chang, Phys. Rev. Lett. 105, 143002 (2010)

Presentations

1) **"Ellipticity dependence of high harmonics generated using 400 *nm* driving lasers**", **Yan Cheng**, Sabih Khan, Kun Zhao, Baozhen Zhao, Michael Chini, Zenghu Chang, 42nd Annual Meeting of the APS Division of Atomic, Molecular and Optical Physics (DAMOP), Atlanta, Georgia (2011)
2) **"Probing autoionization and AC Stark shift with attosecond transient absorption spectroscopy"**, Michael Chini, He Wang, Chang-hua Zhang, Feng He, Shouyuan Chen, **Yan Cheng**, Baozhen Zhao, Yi Wu, Uwe Thumm, Zenghu Chang, 42nd Annual Meeting of the APS Division of Atomic, Molecular and Optical Physics (DAMOP), Atlanta, Georgia (2011)

3) **"Ellipticity dependence of high harmonics from 400 *nm* driving pulses"**, Sabih D. Khan, **Yan Cheng**, Kun Zhao, Michael Chini, Baozhen Zhao, and Zenghu Chang, in CLEO:2011 - Laser Applications to Photonic Applications, OSA Technical Digest (CD) (Optical Society of America, 2011), paper JWA88.
4) **"Attosecond Time-Resolved Autoionization"**, He Wang, Michael Chini, Shouyuan Chen, Changhua Zhang, Feng He, **Yan Cheng**, Yi Wu, Uwe Thumm, and Zenghu Chang, in Quantum Electronics and Laser Science Conference, OSA Technical Digest (CD) (Optical Society of America, 2011), paper QMG3.

References

1. M. Ferray, A. L'Huillier, X. F. Li, L. A. Lompre, G. Mainfray, and C. Manus, "Multiple-harmonic conversion of 1064 nm radiation in rare gases," Journal of Physics B: Atomic, Molecular and Optical Physics **21,** 31 (1988).

2. P. B. Corkum, "Plasma perspective on strong field multiphoton ionization," Phys. Rev. Lett. **71,** 1994-1997 (1993).

3. Z. Chang and P. Corkum, "Attosecond photon sources: the first decade and beyond [Invited]," J Opt Soc Am B **27,** B9-B17 (2010).

4. H. Mashiko, S. Gilbertson, C. Li, E. Moon, and Z. Chang, "Optimizing the photon flux of double optical gated high-order harmonic spectra," Phys. Rev. , A **77,** 063423 (2008).

5. E. L. Falcao-Filho, "Scaling of high-order harmonic efficiencies with visible wavelength drivers: A route to efficient extreme ultraviolet sources," Appl. Phys. Lett. **97,** 061107-3 (2010).

6. E. L. Falcao-Filho, V. M. Gkortsas, A. Gordon, and F. X. K\artner, "Analytic scaling analysis of high harmonic generation conversion efficiency," Opt.Express **17,** 11217-11229 (2009).

7. V. Gkortsas, S. Bhardwaj, E. L. Falcão-Filho, K. Hong, A. Gordon, and F. X. Kärtner, "Scaling of high harmonic generation conversion efficiency," Journal of Physics B: Atomic, Molecular and Optical Physics **44,** 045601 (2011).

8. M. Lewenstein, P. Balcou, M. Y. Ivanov, A. L'Huillier, and P. B. Corkum, "Theory of high-harmonic generation by low-frequency laser fields," Phys. Rev. , A **49,** 2117-2132 (1994).

9. B. Shan and Z. Chang, "Dramatic extension of the high-order harmonic cutoff by using a long-wavelength driving field," Phys. Rev. , A **65,** 011804 (2001).

10. J. Tate, T. Auguste, H. G. Muller, P. Sali\`eres, P. Agostini, and L. F. DiMauro, "Scaling of Wave-Packet Dynamics in an Intense Midinfrared Field," Phys. Rev. Lett. **98,** 013901 (2007).

11. K. Schiessl, K. L. Ishikawa, E. Persson, and J. Burgd\orfer, "Quantum Path Interference in the Wavelength Dependence of High-Harmonic Generation," Phys. Rev. Lett. **99,** 253903 (2007).

12. M. V. Frolov, N. L. Manakov, and A. F. Starace, "Wavelength Scaling of High-Harmonic Yield: Threshold Phenomena and Bound State Symmetry Dependence," Phys. Rev. Lett. **100,** 173001 (2008).

13. A. D. Shiner, C. Trallero-Herrero, N. Kajumba, H. -. Bandulet, D. Comtois, F. L\'egar\'e, M. Gigu\`ere, J. Kieffer, P. B. Corkum, and D. M. Villeneuve, "Wavelength Scaling of High Harmonic Generation Efficiency," Phys. Rev. Lett. **103,** 073902 (2009).
14. S. Gilbertson, M. Chini, S. Khan, Y. Wu, X. Feng, and Z. Chang,"Control of Electron Dynamics of Doubly Excited States from Isolated Attosecond Pulses" in *Conference on Lasers and Electro-Optics*Anonymous (Optical Society of America, 2010).
15. G. Sansone, E. Benedetti, F. Calegari, C. Vozzi, L. Avaldi, R. Flammini, L. Poletto, P. Villoresi, C. Altucci, R. Velotta, S. Stagira, S. De Silvestri, and M. Nisoli, "Isolated Single-Cycle Attosecond Pulses," Science **314,** 443-446 (2006).
16. I. J. Sola, E. Mevel, L. Elouga, E. Constant, V. Strelkov, L. Poletto, P. Villoresi, E. Benedetti, J. -. Caumes, S. Stagira, C. Vozzi, G. Sansone, and M. Nisoli, "Controlling attosecond electron dynamics by phase-stabilized polarization gating," Nat Phys **2,** 319-322 (2006).
17. Z. Chang, "Controlling attosecond pulse generation with a double optical gating," Phys. Rev. , A **76,** 051403 (2007).
18. H. Mashiko, S. Gilbertson, C. Li, S. D. Khan, M. M. Shakya, E. Moon, and Z. Chang, "Double Optical Gating of High-Order Harmonic Generation with Carrier-Envelope Phase Stabilized Lasers," Phys. Rev. Lett. **100,** 103906 (2008).
19. X. Feng, S. Gilbertson, H. Mashiko, H. Wang, S. D. Khan, M. Chini, Y. Wu, K. Zhao, and Z. Chang, "Generation of Isolated Attosecond Pulses with 20 to 28 Femtosecond Lasers," Phys. Rev. Lett. **103,** 183901 (2009).
20. P. B. Corkum, N. H. Burnett, and M. Y. Ivanov, "Subfemtosecond pulses," Opt. Lett. **19,** 1870-1872 (1994).
21. B. Shan, S. Ghimire, and Z. Chang, "Generation of the attosecond extreme ultraviolet supercontinuum by a polarization gating," Journal of Modern Optics **52,** 277-283 (2005).
22. S. Gilbertson, H. Mashiko, C. Li, S. D. Khan, M. M. Shakya, E. Moon, and Z. Chang, "A low-loss, robust setup for double optical gating of high harmonic generation," Appl. Phys. Lett. **92,** 071109 (2008).
23. Zenghu Chang, *Fundamentals of Attosecond Optics*.
24. S. D. Khan, Y. Cheng, M. Moller, K. Zhao, B. Zhao, M. Chini, G. G. Paulus, and Z. Chang, "Ellipticity dependence of 400 nm-driven high harmonic generation," Appl. Phys. Lett. **99,** 161106-3 (2011).

25. e. a. Vasileios-Marios Gkortsas, "Scaling of high harmonic generation conversion efficiency," Journal of Physics B: Atomic, Molecular and Optical Physics **44,** 045601 (2011).
26. I. J. Kim, C. M. Kim, H. T. Kim, G. H. Lee, Y. S. Lee, J. Y. Park, D. J. Cho, and C. H. Nam, "Highly Efficient High-Harmonic Generation in an Orthogonally Polarized Two-Color Laser Field," Phys. Rev. Lett. **94,** 243901 (2005).
27. E. Constant, D. Garzella, P. Breger, E. M\'evel, C. Dorrer, C. Le Blanc, F. Salin, and P. Agostini, "Optimizing High Harmonic Generation in Absorbing Gases: Model and Experiment," Phys. Rev. Lett. **82,** 1668-1671 (1999).
28. Max Möller, Sabih. D. Khan, Yan Cheng, Baozhen Zhao, Kun Zhao, Michael Chini, Gerhard G. Paulus and Zenghu Chang, "Dependence of high harmonic generation yield on driving-laser ellipticity, submitted,".
29. I. M.Y., S. M., and S. O., "Anatomy of strong field ionization," Journal of Modern Optics **52,** 165-184 (2005).
30. M. V. Ammosov, N. B. Delone, and V. P. Krainov, "Tunnel ionisation of complex atoms and of atomic ions in an alternating electromagnetic field," Soviet Physics JETP **64,** 1191 (1986).
31. O. Duhr, E. T. J. Nibbering, G. Korn, G. Tempea, and F. Krausz, "Generation of intense 8-fs pulses at 400 nm," Opt. Lett. **24,** 34-36 (1999).
32. J. Liu, Y. Kida, T. Teramoto, and T. Kobayashi, "Generation of stable sub-10 fs pulses at 400 nm in a hollow fiber for UV pump-probe experiment," Opt.Express **18,** 4664-4672 (2010).
33. J. Liu, K. Okamura, Y. Kida, T. Teramoto, and T. Kobayashi, "Clean sub-8-fs pulses at 400 nm generated by a hollow fiber compressor for ultraviolet ultrafast pump-probe spectroscopy," Opt.Express **18,** 20645-20650 (2010).
34. C. Vozzi, M. Nisoli, G. Sansone, S. Stagira, and S. De Silvestri, "Optimal spectral broadening in hollow-fiber compressor systems," Appl. Phy. B **80,** 285-289 (2005).
35. R. H. Stolen and C. Lin, "Self-phase-modulation in silica optical fibers," Phys. Rev. , A **17,** 1448-1453 (1978).
36. Anonymous "New Port SD-FROG mannual," http://www.newport.com/images/webdocuments-en/images/12246.pdf.
37. Rick Trebino, *Frequency-Resolved Optical Gating: The Measurement of Ultrashort Laser Pulses*, Springer; 1 edition (August 1, 2002)

38. U. Fano, "Effects of Configuration Interaction on Intensities and Phase Shifts," Phys.Rev. **124,** 1866-1878 (1961).
39. H. Wang, M. Chini, S. Chen, C. Zhang, F. He, Y. Cheng, Y. Wu, U. Thumm, and Z. Chang, "Attosecond Time-Resolved Autoionization of Argon," Phys. Rev. Lett. **105,** 143002 (2010).
40. H. Wang, M. Chini, S. Chen, C. Zhang, F. He, Y. Cheng, Y. Wu, U. Thumm, and Z. Chang, "Attosecond Time-Resolved Autoionization of Argon," Phys. Rev. Lett. **105,** 143002 (2010).
41. He Wang, "From Few-cycle Femtosecond Pulse to Single Attosecond Pulse Control and Track Electron Dynamics with Attosecond Precision, Ph.D. Thesis," (2010).